

## Mass-Losing Semiregular Variable Stars in Baade's Windows

C. Alard<sup>1,12</sup>, J.A.D.L. Blommaert<sup>2</sup>, C. Cesarsky<sup>3</sup>, N. Epchtein<sup>4</sup>, M. Felli<sup>5</sup>, P. Fouque<sup>6</sup>,  
S. Ganesh<sup>7</sup>, R. Genzel<sup>8</sup>, G. Gilmore<sup>9</sup>, I.S. Glass<sup>10</sup>, H. Habing<sup>11</sup>, A. Omont<sup>12</sup>, M. Perault<sup>13</sup>,  
S. Price<sup>14</sup>, A. Robin<sup>15</sup>, M. Schultheis<sup>12</sup>, G. Simon<sup>1</sup>, J.Th. van Loon<sup>9</sup>,

*(The ISO GAL Collaboration)*

C. Alcock<sup>16,30</sup>, R.A. Allsman<sup>17</sup>, D.R. Alves<sup>18</sup>, T.S. Axelrod<sup>19</sup>, A.C. Becker<sup>20</sup>,  
D.P. Bennett<sup>21,30</sup>, K.H. Cook<sup>16,30</sup>, A.J. Drake<sup>16</sup>, K.C. Freeman<sup>19</sup>, M. Geha<sup>22</sup>,  
K. Griest<sup>23,30</sup>, M.J. Lehner<sup>24</sup>, S.L. Marshall<sup>16</sup>, D. Minniti<sup>25</sup>, C. Nelson<sup>26</sup>, B.A. Peterson<sup>19</sup>,  
P. Popowski<sup>16</sup>, M.R. Pratt<sup>27</sup>, P.J. Quinn<sup>3</sup>, W. Sutherland<sup>28,30</sup>, A.B. Tomaney<sup>26</sup>, T. Vandehei<sup>23</sup>,  
D.L. Welch<sup>29</sup>

*(The MACHO Collaboration)*

- 
- <sup>1</sup>DASGAL, UMR CNRS N<sup>o</sup> 335, Observatoire de Paris, 21 Avenue de l’Observatoire, Paris F75014, France
- <sup>2</sup>ISO Data Centre, Astrophysic Div., Space Science Dept. of ESA, Apartado 50727, Madrid E28080, Spain
- <sup>3</sup>ESO, Karl-Schwarzschild-Str 2, D-85740, Germany
- <sup>4</sup>Observatory de la Cote d’Azur, Departement Fresnel, BP 4229, F 06304 Nice Cedex 4, France
- <sup>5</sup>Observatory of Arcetri, Largo E. Fermi 5, 50125, Florence, Italy
- <sup>6</sup>ESO, Casilla 19001, Santiago, Chile
- <sup>7</sup>Physical Research Laboratory, Astronomy and Astrophysics Division, Navarangpura, Ahmedabad 380 009, India
- <sup>8</sup>MPE, Karl-Schwarzschild-Str 1, Postfach 1603, D-85740 Garching, Germany
- <sup>9</sup>Institute of Astronomy, The Observatories, Madingley Rd., Cambridge CB3 0HA, United Kingdom
- <sup>10</sup>South African Astronomical Observatory, P.O. Box 9, Observatory 7935, South Africa
- <sup>11</sup>Sterrewacht Leiden, P.O. Box 9513, 2300 RA Leiden, The Netherlands
- <sup>12</sup>Intitut d’Astrophysique de Paris, CNRS, 98bis Blvd Arago, Paris F75014, France
- <sup>13</sup>Laboratoire de Radioastronomie Millimétrique, ENS & CNRS, 24 Rue Lhomond, F-75005 Paris, France
- <sup>14</sup>AFRL, Hanscom AFB, MA, 01731 USA
- <sup>15</sup>Observatoire de Besançon, BP 1615, F-25010 Besançon Cedex, France
- <sup>16</sup>Lawrence Livermore National Laboratory, Livermore, CA 94550, USA
- <sup>17</sup>Supercomputing Facility, Australian National University, Canberra, ACT 0200, Australia
- <sup>18</sup>Space Telescope Science Institute, 3700 San Martin Dr., Baltimore, MD 21218, USA
- <sup>19</sup>Mt. Stromlo and Siding Spring Observatories, ANU, Weston Creek, ACT 2611, Australia
- <sup>20</sup>Departments of Astronomy & Physics, University of Washington, Seattle, WA 98195, USA
- <sup>21</sup>Physics Department, University of Notre Dame, Notre Dame, IN 46556, USA
- <sup>22</sup>Department of Astronomy, University of California, Santa Cruz, CA 95064, USA
- <sup>23</sup>Department of Physics, University of California, San Diego, La Jolla, CA 92093, USA
- <sup>24</sup>Department of Physics, University of Sheffield, Sheffield S3 7RH, United Kingdom
- <sup>25</sup>Departamento de Astronomia, P. Universidad Catolica, Casilla 104, Santiago 22, Chile
- <sup>26</sup>Department of Physics, University of California, Berkeley, CA 94720, USA
- <sup>27</sup>Center for Space Research, MIT, Cambridge, MA 02139, USA
- <sup>28</sup>Department of Physics, University of Oxford, Oxford OX1 3RH, U.K.
- <sup>29</sup>Departments of Physics & Astronomy, McMaster University, Hamilton, Ontario, Canada L8S 4M1.
- <sup>30</sup>Center for Particle Astrophysics, University of California, Berkeley, CA 94720, USA

## ABSTRACT

By cross-correlating the results of two recent large-scale surveys, the general properties of a well defined sample of semi-regular variable stars have been determined. ISOGAL mid-infrared photometry (7 and 15  $\mu\text{m}$ ) and MACHO  $V$  and  $R$  lightcurves are assembled for approximately 300 stars in the Baade’s Windows of low extinction towards the Galactic bulge. These stars are mainly giants of late M spectral type, evolving along the asymptotic giant branch (AGB). They are found to possess a wide and continuous distribution of pulsation periods and to obey an approximate log period – bolometric magnitude ( $\log P - M_{\text{bol}}$ ) relation or set of such relations.

Approximate mass-loss rates  $\dot{M}$  in the range of  $\sim 1 \times 10^{-8}$  to  $5 \times 10^{-7} M_{\odot} \text{ year}^{-1}$  are derived from ISOGAL mid-infrared photometry and models of stellar spectra adjusted for the presence of optically-thin circumstellar silicate dust. Mass-loss rates depend on luminosity and pulsation period. Some stars lose mass as rapidly as short-period Miras but do not show Mira-like amplitudes. A period of 70 days or longer is a necessary but not a sufficient condition for mass loss to occur.

For AGB stars in the mass-loss ranges that we observe, the functional dependence of mass-loss rate on temperature and luminosity can be expressed as  $\dot{M} \propto T^{\alpha} L^{\beta}$ , where  $\alpha = -8.80_{-0.24}^{+0.96}$  and  $\beta = +1.74_{-0.24}^{+0.16}$ , in agreement with recent theoretical predictions.

If we include our mass-loss rates with a sample of extreme mass-losing AGB stars in the Large Magellanic Cloud, and ignore  $T$  as a variable, we get the general result for AGB stars that

$$\dot{M} \propto L^{2.7},$$

valid for AGB stars with  $10^{-8} < \dot{M} < 10^{-4} M_{\odot} \text{ yr}^{-1}$ .

## 1. Introduction

One of the most complex and least understood phases of stellar evolution is the asymptotic giant branch (AGB; Iben & Renzini 1983). AGB evolution is regulated by very high rates of mass loss (Bowen & Willson 1991; Vassiliadis & Wood 1993).

The current theory of mass loss from red giants invokes a combination of two physical processes: stellar pulsation and radiation pressure on dust grains (see reviews by Morris 1987; Gail, Kuntz & Ulmschneider 1990; Lafon & Berruyer 1991; Habing 1996). The association of mass loss with pulsation is due to the fact that mass-losing red giants are often variable stars, such as Miras, and the mass-loss rates of Miras are observed to be correlated with their pulsation periods (de Gioia-Eastwood et al. 1981; Whitelock et al. 1994, 1995). Stellar pulsation is theoretically linked to mass loss through the propagation of periodic shocks (Wood 1979; Willson & Hill 1979). The shocks are nearly isothermal, and thus responsible by themselves for very low mass-loss rates (Bowen 1988). However, they also extend the outer-atmospheres of red giants, increasing the gas density at the dust condensation radius. Dust therefore forms efficiently, and radiation pressure accelerates the dust grains (Hoyle & Wickramasinghe 1962). The accelerated dust grains are momentum-coupled to the gas, which drives mass loss at high rates (Gilman 1972; Kwok 1975). The standard theory of mass loss has evolved to include sophisticated treatments of time-dependent hydrodynamics, grain condensation, and radiative transfer (e.g. Fleischer, Gauger & Sedlmayr 1992; Arndt, Fleischer & Sedlmayr 1997).

The standard theory of mass loss in red giants may not be appropriate for all AGB stars. While the majority are variable (e.g. Alcock et al. 2000), most do not show the large-amplitude, long-period pulsations characteristic of Miras. Instead, most AGB variable stars are classified as semiregulars (SRs). The classical requirement for a Mira is that it shows an optical pulsation amplitude  $\Delta V > 2.5$  mag, while the semiregulars are defined as having pulsation amplitudes smaller than this. Stars with visual amplitudes around the dividing level occur relatively infrequently (Payne-Gaposchkin, 1951). The optical pulsation amplitudes of current model AGB stars with periodic shocks as prescribed by the theory of mass loss are typical of the pulsation amplitudes of Miras, but not of semiregulars. Another characteristic feature of Miras is periodic Balmer-line emission, believed to arise from shocks (Willson 1976). The theoretical velocity changes across the periodic shocks are in agreement with those inferred from the Balmer-line emission of Miras (Fleischer, Gauger & Sedlmayr 1992). Although data are scarce, many SRs do not exhibit periodic Balmer-line emission. In addition, near-infrared spectra of SRs do not show line-doubling as Miras often do, a characteristic of shocks (Hinkle, Lebzelter, & Scharlach 1997). Thus the pulsations induced in the standard theory of mass loss are probably too strong to be appropriate for semiregulars.

Up till now, detailed knowledge of the properties of the SR variables has been limited to relatively small numbers of bright objects, mainly situated in the solar neighborhood at unknown distances (e.g. Jura & Kleinmann 1992; Kahane & Jura 1994; Kerschbaum, Olofsson

& Hron 1996; Mennessier et al. 2000). However, the picture is undergoing rapid change thanks to the gravitational lensing experiments like MACHO and OGLE, and the astrometric satellite Hipparcos, which have obtained frequent photometric measurements of large samples of SRs at known distances, and over long periods of time. These relatively new databases cover well-defined samples and can reveal variations with amplitudes as small as a few hundredths of a magnitude, well beyond the capabilities of earlier photographic work. We mention Alves et al. (1998), Minniti et al. (1998), Wood et al. (1999), and Glass et al. (2000) who have discussed MACHO observations of SRs in the LMC and Galactic Bulge. Koen & Laney (2000), Bedding & Zijlstra (1998), and others have discussed SRs observed by Hipparcos in the solar neighborhood.

At the same time, the ISOCAM camera of the Infrared Space Observatory (ISO)<sup>31</sup> pointed, observatory-style satellite has enabled mid-infrared photometric surveys to be carried out with much greater sensitivity and spatial resolution than, for example, was possible with IRAS, which suffered severely from crowding of sources near the Galactic plane. In particular, in the Baade’s Windows of low extinction in the inner part of the Galactic bulge, the ISOGAL Collaboration has detected 1193 stars in the ISOCAM  $7\mu\text{m}$  or  $15\mu\text{m}$  bands in two fields of  $15 \times 15$  arcmin<sup>2</sup> (Glass et al. 1999). As a result, it is now evident that there is a continuous sequence of increasing mass-loss from mid- to late-type M-giant stars on the AGB, ending with the Miras and other long-period, large-amplitude variables.

In order to advance our theories of AGB stellar evolution, and in particular, advance our understanding of mass loss, we have undertaken a new study of AGB stars in the Galactic bulge. We have combined two types of observations ideally suited to investigate issues of AGB star mass loss: optical-band lightcurves from the MACHO Project and mid-infrared photometry from the ISOGAL Collaboration. Our dataset is the first large sample of mass-losing AGB variable stars whose pulsation and mass-loss rates are well-characterized, and whose distances, and thus energetics, are also known.

## 2. Data

### 2.1. ISOGAL

The ISOGAL Survey<sup>32</sup> is a multi-wavelength infrared survey of the inner Galaxy at high resolution (Omont et al. 2000). It made use of the ISOCAM camera (Cesarsky et al. 1996) on the ISO satellite to survey numerous sample fields in visually-obscured regions along the Galactic plane and towards the center of the Galaxy in order to study topics such as Galactic structure,

---

<sup>31</sup>ISO is a European Space Agency (ESA) project with instruments funded by member states (especially the PI countries: France, Germany, the Netherlands, and the United Kingdom) and with the participation of ISAS and NASA.

<sup>32</sup>This is paper no. 10 in a refereed journal based on data from the ISOGAL Survey.

the red giant population, interstellar extinction and other matters.

### 2.1.1. ISOGAL observations

The survey comprises mainly exposures in the LW2 (5.5–8 $\mu$ m) and LW3 (12–18 $\mu$ m) broad-band filters of ISOCAM. Each pixel subtended 6  $\times$  6 arcsec<sup>2</sup> on the sky. The detector arrays had 32  $\times$  32 pixels. Large areas could be imaged by combining individual images obtained during raster scans. The data that we describe were obtained from two areas located in the Baade’s Windows, each covering 15  $\times$  15 arcmin<sup>2</sup> in  $\ell, b$ . Exposures were made on two occasions, about a year apart (see Glass et al. 1999). On the first occasion, observations were obtained only with the LW2 filter; on the second, both filters were used. The centres of the fields were at  $\ell = +1.03^\circ$ ,  $b = -3.83^\circ$ , which includes the globular cluster NGC 6522, and at  $\ell = +1.37^\circ$ ,  $b = -2.63^\circ$ , known as the SgrI field. The Baade’s Window fields were included because, although they are near the galactic centre, they are sufficiently unobscured (with visual extinction  $A_V \sim 1.5 - 1.8$  mag) to be observable at visual wavelengths and have been the subject of numerous previous investigations. Thus they can be regarded as fiducial fields for the analysis of more heavily obscured areas.

### 2.1.2. Photometric properties

ISOGAL has identified 1193 sources from these fields at either or both of the 7- and 15-micron passbands. In the fields Sgr I and NGC 6522, there are 696 and 497 sources, respectively. Of these, 182 and 287 were detected at both wavelengths. The methods used for reducing the photometry, taking account of various difficulties produced by the responses of the detectors and the crowded nature of the fields, have been described by Glass et al. (1999). The flux calibrations of the 7  $\mu$ m and 15  $\mu$ m bands were set for a spectrum with  $F_\lambda \propto \lambda^{-1}$  and should be correct at wavelengths 6.7 and 14.3  $\mu$ m respectively. Conversion from magnitudes follows the relations

$$[7] = 12.38 - 2.5 \log F_{LW2}(\text{mJy}) \quad (1)$$

and

$$[15] = 10.79 - 2.5 \log F_{LW3}(\text{mJy}), \quad (2)$$

where the zero points have been set to obtain zero mag for a Vega model flux at the isophotal wavelengths given above.

Only sources with fluxes greater than 5 mJy in either or both filters were accepted for the final catalogue. These limits correspond to  $[7] = 10.64$  and  $[15] = 8.99$ . The rms dispersion of the ISOGAL photometry is 0.14–0.2 mag, except at the faint end, where it rises to  $\sim 0.4$  mag (see Glass et al. 1999; Ganesh et al. in preparation). With 35–45 pixels per source, observations in these fields are seen to be close to the confusion limit.

As in Glass et al. (1999), we have not applied extinction corrections to the ISOGAL data. The absorption in the ISOGAL bands is believed to be less than 0.05 mag, though the precise character of the interstellar extinction curve in this wavelength region is not well-determined.

### 2.1.3. Astrometric calibration

The extracted source positions were set systematically by reference to the Deep Near-Infrared Survey (DENIS) positions for the same area. The DENIS survey has an internal astrometric accuracy of order  $0.5''$  (see Omont et al. 1999) and is ultimately referred to the USNO-A2.0 astrometric catalogue, which has a rms absolute accuracy of 1 arcsec. The rms dispersions of the differences between the ISOGAL and the DENIS positions are (0.6, 0.7) and (0.9, 0.8) arcsec in (R.A., Dec) for NGC 6522 and Sgr I, respectively.

### 2.1.4. ISOGAL color-magnitude diagram

Figure 1 shows the color-magnitude diagram (CMD) for 182 and 287 stars detected at both wavelengths in NGC 6522 and Sgr I fields, respectively. The objects in the Baade’s Windows are almost exclusively from the Bulge, and are therefore at a nearly constant distance from the Sun, with a distribution governed by the thickness of the Bulge. The minimum photometric scatter due to line-of-sight effects can be expected to be similar to that derived from the period– $K$  luminosity plot for Miras in the Sgr I field (Glass et al. 1995), viz 0.35 mag, since the intrinsic scatter in the relationship is known to be  $\leq 0.13$  mag from Magellanic Cloud studies (Glass et al. 1987). There is a continuous progression of [15] mag, and therefore dust output, with [7]–[15] color and late spectral type (Glass et al. 1999). The sequence stretches from the top of the Red Giant Branch (RGB), located in the bottom left corner of the diagram, to the Mira variables, which are generally, but not exclusively, the most luminous dust emitters. Mira-type large-amplitude variability is thus seen not to be a necessary condition for mass-loss in M-stars, as was previously believed.

The objects which approach the Miras in dust emission are close to them in  $K$ -mag also (Frogel & Whitford 1987; Glass et al. 1999), indicating that they have similar bolometric mags. Spectral types are available for all the M-giants in part of the ISOGAL NGC 6522 field (Blanco 1986), as well as for late-type M-giants in the whole field (Blanco, McCarthy & Blanco 1984). It is evident from figure 12 of Glass et al. (1999) that only M5 giants or later types are detectable at  $15\mu\text{m}$ , i.e., it is only these objects that have observable dust shells. Mira and SR variables of C-type are entirely absent from these fields.

A group of stars with luminosities similar to Miras, marked by crosses in Figure 1, were examined by T. Lloyd Evans on the photographic plate material that was used for finding most of the known Miras in the Baade’s Window fields (Lloyd Evans 1976). Little additional evidence was

found for photometric variability, ruling out the notion that they may have been overlooked as Miras, but not excluding the possibility that they could be SR variables of much lower amplitude. It therefore became of interest to see if a modern photoelectric survey would reveal anything more.

## 2.2. MACHO

The MACHO Project had dedicated use of the 50-inch Great Melbourne Telescope located at the Mount Stromlo Observatory in Australia from January, 1992 to January, 2000. A system of corrective optics installed at the prime focus gave a focal reduction to  $f/3.9$  and a  $1^\circ$  field of view. A dichroic beam-splitter enabled simultaneous blue and red imaging. The MACHO filters were non-standard, with the blue filter running from  $\sim 4500\text{--}6300 \text{ \AA}$  and the red filter from  $\sim 6300\text{--}7600 \text{ \AA}$  (see Alcock et al. 1999). At both the red and blue foci, a mosaic of four  $2048 \times 2048$  Loral charge coupled devices (CCDs) were mounted, yielding an  $0.52$  square degree imaged area.

Approximately  $45$  square degrees of the Galactic bulge were observed every few nights, with exceptions for weather and the southern summers. Photometry was handled by a special purpose crowded-field, PSF-fitting code called SoDOPHOT, which is described by Alcock et al. (1999). At the time of this work, the MACHO photometry database contained a time-series of  $\sim 1000$  two-color photometric measurements spanning  $\sim 6$  years for most Galactic bulge fields. Most of the stars of interest here are quite bright, and thus the typical error on each photometric measurement is about  $\pm 0.02$  mag.

Following Alcock et al. (1999), the MACHO instrumental photometry have been calibrated to the standard Kron-Cousins system using:

$$V = v + 23.699 - 0.1804 (v - r) \quad (3)$$

$$R = r + 23.412 + 0.1825 (v - r) \quad (4)$$

where  $v$  and  $r$  are instrumental magnitudes, and  $V$  and  $R$  are on the Kron-Cousins standard system. The color coefficients are averages of the values determined for different CCDs in the MACHO focal plane, corrected for airmass. These calibration formulae are estimated to have an overall absolute accuracy of  $\pm 0.10$  mag in  $V$  or  $R$ , and  $\pm 0.04$  mag in  $(V - R)$ . For the purposes of calibration, we assumed  $(v - r) = 0.5$  mag for all stars without instrumental colors in the database; the systematic error may be larger for these stars. The systematic calibration error may also be larger for stars with colors of  $(V - R) > 1.2$  mag (see Alcock et al. 1999).

Astrometry for the MACHO database was derived independently for each field using the Guide Star Catalog. Astrometric offsets of order  $\sim 1''$  between MACHO fields (as determined from common stars in field overlap regions) are typically found, which gives an indication of the overall astrometric accuracy to be expected.



### 3. Matching MACHO & ISOGAL Sources

In our initial reconnaissance of the MACHO photometry database, we overplotted MACHO “tiles” on the spatial distribution of ISOGAL sources (tiles are a defined region of the sky in the MACHO database, each approximately a few arcminutes square). In this manner, we identified 54 tiles that overlapped (or nearly overlapped) ISOGAL sources. Unique starlists were extracted from the MACHO photometry database for these tiles, which totaled just over  $3 \times 10^5$  stars. We estimate that 91% and 88% of the areas of the ISOGAL SGR I and NGC 6522 fields, respectively, are included in the MACHO photometry database. This estimate accounts for gaps in MACHO sky coverage between fields and CCDs, but not for area lost to CCD defects or saturated pixels. The latter probably accounts for no more than  $\sim 5\%$  of the field area.

A blind spatial matching of the ISOGAL sources with such a large number of MACHO stars would have certainly resulted in numerous chance coincidences. Therefore, we decided to apply a “reasonable” cut in the optical color-magnitude diagram before attempting to cross-correlate sources. We considered only MACHO stars with  $V > 13.5 + 4.67(V - R)$  as possible counterparts to the ISOGAL sources. This cut was chosen to include the red clump, very red faint stars, and very bright blue stars. It excluded most faint main sequence stars, but may have also excluded some relatively blue AGB stars located behind the Galactic bulge. After applying this cut, approximately  $4 \times 10^4$  MACHO stars remained.

For each of the 1193 ISOGAL sources, the angular distance to each MACHO star was calculated, and the closest positional match was recorded if lying within 3 arcseconds. In an initial matching trial, median offsets in  $\alpha$  and  $\delta$  were calculated using a subset of matches that included only MACHO stars with colors  $(V - R) > 1.5$  mag, which were considered very likely matches. The offsets for each field, in the sense of ISO – MACHO, and in units of arcseconds, are:  $(\Delta\alpha, \Delta\delta) = (1.4, 0.7)$ , and  $(0.8, 0.6)$  for ISOGAL fields SGR I and NGC 6522, respectively. A second and final matching trial proceeded as the first, except that the offsets were applied.

Figure 2 shows the final distribution of angular separations for matches in ISOGAL fields SGR I and NGC 6522. In order to provide some estimate of the number of spurious matches, we repeated the matching procedure described above, except that we applied an arbitrary ( $\sim 15$  arcsec) shift to each MACHO starlist. The result of this control matching trial is also shown in Figure 2 (shaded histograms). The total number of matches are 518 and 386 in ISOGAL fields SGR I and NGC 6522, while the probabilities for a spurious match are 7% and 3%, respectively. The details of the matching criteria described above do not affect the main results of this work.

The total number of matches (904) represents 76% of the 1193 ISOGAL sources, which compares to the estimated  $\sim 90\%$  overlapping area between the MACHO and ISOGAL fields. This discrepancy ( $\sim 165$  stars) is probably too large to attribute to CCD defects in the MACHO images, which would tend to lower the percentage of overlapping area ( $\sim 5\%$ ). It would also seem too large to attribute to saturation in the MACHO data ( $V_{SAT} \sim 11$ ; although this is certainly case for some known Miras, as discussed below). It is unlikely that this represents a significant

population of self-obscured AGB stars, since there aren't that many very bright ISOGAL sources. It is possible that the ISOGAL sources without optical counterparts are not real, but are instead low signal-to-noise, false detections. However, a combination of all of the above effects is perhaps the most likely explanation. A detailed accounting of each ISOGAL source is beyond the scope of this work. We are confident that we have correctly matched a large number of ISOGAL sources with MACHO stars, and will proceed with an analysis of this dataset.

332 stars of the 904 MACHO and ISOGAL matches have complete sets of  $V$ ,  $R$ , [7], and [15] mags. They are listed in Table 1. In Figure 3, we plot all 904 sources, distinguishing those with four-color photometry. The four-color sources are seen to deviate in the direction of higher  $V - R$  and/or fainter  $V$  from the others, apart from the small group of stars near  $V \sim 17$ ,  $V - R \sim 0.9$ , which coincide with the red giant clump. This can be an effect of either or both of photospheric temperature and reddening due to circumstellar material. Those located near the clump are consistent with chance matches.

For the remainder of this work, we restrict our analyses to the subset of 332 matches with four-color photometry.

## 4. Pulsation characteristics

### 4.1. Periodicity

Most of our sample (305 out of 332, or 92%) show quite well-defined periodic or quasi-periodic variations of moderate amplitude superimposed on irregular longer-term fluctuations, which do not, with a few exceptions, appear periodic on the overall time scale of our observations. Of the remaining 27 stars, 26 were frequently saturated in the MACHO image data and thus have unusable light curves. The remaining object is an eclipsing binary. There are 14 known Miras in these fields and they are discussed separately below. The SRs outnumber the Miras by about 20:1.

### 4.2. Semiregular Variables

All 332  $R$ -band light curves were plotted and examined. Approximate periods were first estimated by eye and later made more precise by Fourier analysis. The seasonality of the observations led to the presence of confusing noise at low frequencies as well as aliases. Stars with estimated values of  $\log P < 2.2$  were analysed separately from those with longer periods.

The  $\log P < 2.2$  stars (280) were Fourier analysed season by season and their amplitude periodograms were then summed. The component with highest amplitude with  $\log P < 2.2$  was taken to be the most characteristic or relevant one, even if other periods sometimes had almost equal amplitudes.

The remaining 25 of the 305 periodic or quasi-periodic variables, i.e., those with estimated  $\log P \geq 2.2$ , were also Fourier analysed, but using the information derived by eye from the light curves to assist in the interpretation.

It is traditional to divide the SR variable giants, whether having M-, C-, or S-type spectra, into subtypes SRa and SRb, according to their variability characteristics. The SRa types show persistent periodicity in the range 35–1200 days, though with amplitudes less than Miras (defined to have minimum amplitude  $>2.5$  mag at  $V$ ) and variability in amplitude and light-curve shapes. The SRb stars have much more poorly expressed periodicity in the range (20–2300) days, with slow, irregular changes, or even periods of constancy. Usually, however, a mean period can be assigned to them.

About 3/4 of our variables can be classified as SRa and most of the remainder as SRb. However, this classification scheme can only be regarded as subjective. The SRb types occur predominantly among the longer-period objects.

Figure 4 (a) – (d) shows examples of the different types of variables.

### 4.3. Mira Variables

Of the fourteen Miras known from previous work (Lloyd Evans, 1976; Glass et al. 1995), six have good to recognizable Mira light curves (Table 2). Five were completely missing from the overall list of 332 identifications because they were saturated in the MACHO template images for these fields and thus do not appear at all in the MACHO photometry database (Alcock et al. 1999). The remaining three were misidentified and *do* appear amongst the 332, but as matches to nearby faint stars. The Miras themselves were saturated in the MACHO images. Two of the resulting three ‘wrong’ light curves exhibit irregular flare-like spikes which presumably arise from occasional seeing-related contamination from the true Mira counterparts.

The periods determined by MACHO are based on much more comprehensive light curves than either those of Lloyd Evans (1976) or Glass et al. (1995). It is therefore interesting to compare these values in order to have some check on the error arising from uncertain  $P$  values when determining  $P - L$  relations. The differences may be due to observational error or to intrinsic irregularities in the Mira light curves (Fig 4a). For the 6 stars in common with Lloyd Evans (1975) we find  $\Delta P/P_{\text{MACHO}} = 7 \pm 5\%$  and for the 4 stars in common with Glass et al. (1995) we get  $\Delta P/P_{\text{MACHO}} = 9 \pm 9\%$ . Since the scatter of the LMC Miras around their  $K, \log P$  relation is around 13%, it is clear that errors arising from uncertain or poorly determined periods contribute significantly to the overall scatter in the relationship, besides those associated with finding the mean values of  $K$ .

#### 4.4. Period-Luminosity Relations for Semiregulars and Miras

Fig 5a shows the  $\log P$ , [7] diagram for our sample. As we will see, the  $7\mu\text{m}$  mag is, like the  $K$ , closely related to  $M_{\text{bol}}$  for these stars. We have superimposed a line equivalent to that which fits local SR variables having photometric and astrometric data from Hipparcos, as suggested by Bedding and Zijlstra (1998). To transform from their empirical  $M_K$  relation to one involving [7], we made use of 51 late-type non-Mira stars in the NGC 6522 Baade’s Window having  $K_0$  (de-reddened) values by Frogel & Whitford (1987) and also  $7\mu\text{m}$  mags from ISOGAL, finding that  $[7] = 1.04 K_0 - 0.20$  (s.d. 0.26). (For reference, using Frogel & Whitford’s (1987) bolometric magnitudes corrected for the difference in assumed distance moduli, we also found  $M_{\text{bol}} = 0.75 [7]_{\text{obs}} - 9.25$  (s.d. = 0.21) for the same sample. The distance modulus of the Baade’s Windows was taken to be 14.7 in our work and 14.2 by Frogel & Whitford). The Bedding and Zijlstra (1998) line then has the form

$$[7] = -1.85 \log P + 11.27. \quad (5)$$

The Bedding & Zijlstra (1998) line runs fairly centrally through, or perhaps 0.1 to 0.2 mag above, the distribution of Baade’s Window points. It is about 0.8 mag above that originally found for globular cluster variables with periods in the range  $0 \leq \log P \leq 2.8$  by Whitelock (1986).

Fig 5a also includes an empirical  $\log P$ , [7] fit for the Miras, excluding TLE 57 (a possible SR):

$$[7] = (-6.9 \pm 1.4) \log P + (23.5 \pm 3.4), \quad (6)$$

with s.d. 0.4. Unlike the case for the SR variables, the  $7\mu\text{m}$  flux from a Mira is likely to include a substantial component arising from dust as well as normal photospheric emission. It is therefore no longer a simple measure of bolometric output, particularly at longer periods.

The  $K$  emission of Miras is little contaminated by dust and *is* thus more representative of bolometric output. Accordingly, in order to facilitate a more direct comparison with other work, in Fig 5b we have transformed the [7] mags of the SRs to  $K_0$  and plotted a  $\log P$ ,  $M_K$  diagram, with the Bedding and Zijlstra (1998) line and the same authors’ transformation of the Whitelock (1986) fit (its exact position is dependent on the distance scale used).

Fig 5c shows the  $\log P$ ,  $M_{\text{bol}}$  diagram, where we have transformed the [7] mags of the SRs to  $M_{\text{bol}}$  using the relationship given above. The Miras and their  $P - L$  relation from Glass et al. (1995) are shown, as is the (linear)  $P$ ,  $M_{\text{bol}}$  relation given by Whitelock (1986) for Galactic globular clusters.

The shallow sequence of SRs relative to the Miras in these diagrams (Figs 5a,b,c) may reflect an evolutionary sequence. Evolutionary tracks of this kind, though covering a much reduced period range ( $1.8 < \log P < 2.8$ ), were predicted by Vassiliadis & Wood (1993). Alves et al. (1998) have also projected theoretical evolutionary tracks onto the PL diagram, extending the sequences to the lower luminosities and shorter periods appropriate for SRs. The Alves et al. (1998) PL sequences are based on accurate analytic approximations to the grid of Vassiliadis & Wood (1993)

AGB models and are thus properly comparable to the latter authors’ PL sequences. The absolute luminosities of the evolutionary PL sequences depend on initial mass and metallicity. Alves et al. (1998) showed that SRs in the clusters 47 Tuc and NGC 1783, which have similar metallicities but different initial masses, support the relative luminosities predicted by the theoretical PL sequences. Therefore, the overall luminosity of the SRs in Fig. 5a,b,c may indicate the characteristic age and metallicity of the AGB population.

When a star moves up along one of the nearly parallel evolutionary sequences in the PL diagram, it eventually reaches the Mira line at a unique position. For Galactic globular clusters, this occurs at the relatively short period of about 200 days, in accordance with the known period distribution of the Miras that they contain. The solar neighbourhood line intersects the Miras at about 460 days. The period distribution of local Miras is unknown at present, but long periods are common and this figure may be reasonable. The census of Miras in the Sgr I Baade’s Window is complete (Glass et al. 1995) and their average period is 346 days, in accord with the distributions in Fig. 5a,b,c. This period is much longer than the typical 200 days found for Miras in Galactic globulars and is consistent with the SRs in Baade’s Window lying above the Whitelock (1986) PL sequence.

It is known that the scatter of the Miras in the Sgr I Baade’s Window around the  $\log P, K_0$  relation is  $\sim 0.35$  mag (Glass et al. 1995). Most of this is attributed to the distribution of the Miras along the line of sight, i.e., the finite thickness of the Bulge, though some of it may be caused by the patchy nature of the interstellar extinction. The scatter of the SR variables in Fig. 5a is not much greater, implying that the spread of evolutionary tracks cannot be very wide.

As can be seen from Fig. 6 (upper panel), there is no conspicuous clumping in numbers at any given period of the semiregular variables in our sample. There is however a gap visible in Fig. 5a,b,c between the Mira region and the semi-regular variables similar to that noted by Wood & Sebo (1996) and Wood (2000) in the case of the Large Magellanic Cloud. This gap corresponds, however, to the period range where aliasing is severe due to the seasonality of the MACHO data, and may in part be an artefact. Wood & Sebo (1996) and Wood (2000) interpret the Mira sequence as being one of fundamental mode pulsators and suggest that the semi-regulars pulsate in higher modes. First overtone pulsators are expected to lie on a parallel sequence about  $\Delta \log P \sim 0.35$  to the left of the fundamental, and higher modes should lie at progressively smaller intervals to the left of these. The sequences arising from the higher modes, although clearly seen in the LMC, are not expected to be separated from each other as clearly in our Baade’s windows data because of greater observational error and a range of distances. The necessity that the short-period end of the semi-regular M-giants must pulsate in very high modes has also been discussed by Koen & Laney (2000). This interpretation is not incompatible with the evolutionary picture previously discussed.

#### 4.5. Amplitudes

Because the short-period variability of the SRs is often modulated by apparently irregular long-period trends, eye-estimates of the envelope of the  $R$ -band variations were made for each star, accurate to about 20% or 0.05 mag, whichever is greater. None exceeded  $\Delta R \sim 1$  mag, whereas the five Miras with adequate data (Fig. 4a) each showed  $\Delta R \sim 4$  mag.

Three stars with short periods around 50 – 60 days also showed long periods around 400 days (one or two other short-period stars are also suspected to have long periods close to a year, but their interpretation is confused by the annual nature of the observations). They have amplitudes of 0.1 – 0.2 mag in the short periods and 0.5 mag in the long (see Fig. 4d), but have luminosities appropriate to SRs rather than Miras. Similar stars are found in the LMC MACHO data (see Alves et al. 1998; Wood et al. 1999), covering short periods of 50 – 100 days and long periods of 250 – 1000 days. Wood et al. find long to short period ratios in the range 5 – 13.

Figure 6 shows a histogram of the average amplitude of variability as well as the period distribution. There is a very clear trend towards smaller amplitudes at shorter periods (see also Minniti et al. 1998). The shorter period groups may have been influenced by selection effects, in the sense that very small amplitude variables may not have been detected.

### 5. Discussion of mass-loss rates

In non-Mira M-giant stars, the flux entering the  $7\mu\text{m}$  ISOCAM LW2 filter arises primarily from photospheric emission and does not include a large dust contribution. The  $15\mu\text{m}$  LW3 filter, on the other hand, overlaps with the silicate dust emission features at 10 and  $18\mu$  and is strongly affected by dust, when present. Only when the dust is optically thick, such as in long-period Miras and OH/IR sources, is the  $7\mu\text{m}$  band likely to be strongly affected. The  $K_0$  and [7] mags of the SRs and Miras previously discussed in §4.4 are consistent with this scenario.

#### 5.1. Spectral Energy Distributions

Here we model the spectral energy distributions (SEDs) for the small subset of our sample also identified by Frogel & Whitford (1987). These stars allow us to calibrate mass-loss rates based upon the observed  $15\mu\text{m}$  flux excess using model SEDs. We also attempt an initial characterization of how mass-loss rates depend on fundamental stellar parameters such as luminosity and effective temperature in order to compare with recent theoretical predictions. This is the first time that dust sensitive mid-infrared photometry has been assembled for a sample of SRs (and Miras) whose distances and thus energetics are known. We compare pulsational properties of the sample with mass-loss rates calibrated here in §5.4.

First, we assembled  $J_0$  and  $K_0$  photometry (see also Table 2) and SED-integrated bolometric magnitudes for 26 stars (1 Mira from Table 1 and 25 SRs from Table 2) from Frogel & Whitford (1987). The bolometric magnitudes were adjusted by  $-0.5$  mag to account for a distance modulus of 14.7 mag as discussed previously. The ISOGAL running number (BW), the MACHO identifier, the star name by Frogel & Whitford (1987) and the adjusted values of  $M_{\text{BOL}}$  are listed in the first four columns of Table 3, respectively. The  $V$  and  $R$  magnitudes were dereddened by adopting a visual extinction of  $A_V = 1.5$  mag and taking  $A_R/A_V = 0.75$ . Optical and near-infrared fluxes were calculated using the zero points from Bessell, Castelli, & Plez (1998). The mid-infrared fluxes were calculated from Eqns. (1) & (2) of this paper. Errors associated with absolute flux calibration and dereddening are negligible for the purposes of this work.

Stellar effective temperatures in column (5) of Table 3 were calculated from the dereddened  $(V - K)_0$  color, where we employed the calibration of Bessell, Castelli, & Plez (1998). These temperatures are assumed to represent an accurate, relative effective temperature scale. It is noted that systematic uncertainty in the temperature scale at the  $\pm 100^\circ\text{K}$  level or less will not affect our conclusions (e.g., see §5.2).

For our SED modeling, we assembled the “corrected” model spectra of Lejeune, Cuisinier, & Buser (1997) with solar  $[\text{Fe}/\text{H}]$ ,  $\log g$  of either 0.28 or 0.00, and effective temperatures of 2500, 2800, 3000, 3200, 3350, 3500, 3750, and 4000 °K. This was the finest temperature grid available. This corrected spectral library, by definition, yields synthetic optical and near-infrared broadband colors consistent with the  $(V - K)_0$  color-temperature calibration adopted above. We caution that these model spectra are for static stars and do not take account of photospheric extension arising from variability (e.g., Bessell et al. 1989).

The Lejeune et al. (1997) model spectra were input as  $\lambda$ ,  $F_\nu$  files into the radiative transfer code, DUSTY (Ivezić, Nenkova, & Elitzur 1999). DUSTY solves the radiative transfer problem of an AGB star enshrouded in dust, including a self-consistent solution for the density structure in the wind-driven dust shell. We adopted the faster-running analytic approximation for the wind-driven dust density structure, which is an option in DUSTY. We chose 100% warm silicate for the grain composition (Ivezić et al. 1999). The grain size distribution was a truncated power-law ( $q = -3.5$ ,  $a_1 = 0.005 \mu\text{m}$  and  $a_2 = 0.25 \mu\text{m}$ ; Ivezić et al. 1999; see also Mathis, Rumpl, & Nordsieck 1977). The temperature at the dust shell’s inner-boundary was fixed to be 1000 °K, which is supported by observations (Reid & Menten 1997). We ran a total of  $\sim 200$  model SEDs with DUSTY using the 8 different Lejeune et al. (1997) model spectra as inputs and allowing for a wide range of mass-loss rates. DUSTY reports the mass-loss rate ( $\dot{M}_{L4}$ ) and the expansion velocity ( $V_{exp}$ ) normalized to a luminosity  $L = 10^4 L_\odot$ . The true mass-loss rate ( $\dot{M}$ ) scales in proportion to  $L^{3/4}$  and  $(r_{gd}\rho_s)^{1/2}$ , where  $r_{gd}$  is the gas-to-dust ratio and  $\rho_s$  is the dust grain bulk density. The expansion velocity scales as  $L^{1/4}$  and  $(r_{gd}\rho_s)^{1/2}$ . For these latter parameters, the default values from DUSTY are employed:  $r_{gd} = 200$  and  $\rho_s = 3 \text{ g cm}^{-3}$ . This corresponds to an absorption coefficient at 60  $\mu\text{m}$  of  $\chi_{60} = 70 \text{ cm}^2 \text{ g}^{-1}$ . For all stars, we assume that  $r_{gd}$ ,  $\rho_s$ , the grain size distribution, the dust composition, and the temperature at the inner-boundary are the

same. These simplifying assumptions are sufficient to establish a plausible, relative calibration of the mass-loss rates in our sample.

Each model SED from DUSTY is fit to the observed, deredded flux data in the  $\log(\lambda F_\lambda)$  versus  $\log(\lambda)$  plane, allowing for one zeropoint constraint. The SED fits yield both the luminosity and temperature. The best-fit input model spectrum temperature ( $T_{\text{MOD}}$ ) and the mass-loss rate normalized to  $L = 10^4 L_\odot$  ( $\dot{M}_{L4}$ ) are listed in columns (6) & (7) of Table 3, respectively. The true mass-loss rate ( $\dot{M}$ ), which is rescaled for each known stellar luminosity by a factor of  $(L/10^4 L_\odot)^{3/4}$ , is listed in column (8) of Table 3. Finally, the expansion velocity corrected for a factor of  $(L/10^4 L_\odot)^{1/4}$  is listed in column (9) of Table 3.

We find reasonable agreement between the  $(V - K)_0$  color temperatures and those indicated by the best-fit model SEDs. However, the former are preferred because of the poor temperature resolution of the grid of model spectra. We also checked that the stellar luminosities derived from our SED fits agree with those taken from Frogel & Whitford (1987). The agreement is fair in most cases. However, in a few instances of fitting the SEDs of stars with high mass-loss rates, we obtain luminosities lower than those given by Frogel & Whitford (1987). In these cases, our statistical best-fit model SED (which gives equal weight to all flux data) underestimates the near-infrared flux (near the peak of  $\lambda F_\lambda$ ) and overestimates the mid-infrared data. Fortunately, while this affects the luminosities so obtained, the mass-loss rates themselves are not underestimated at a level which is important in this work. In summary, we adopt the distance modulus-adjusted, SED-integrated Frogel & Whitford (1987) luminosities, the Bessell, Castelli, & Plez (1998)  $(V - K)_0$  color temperatures, and the SED-fit mass-loss rates in our subsequent analyses.

Figure 7 shows four example SEDs (filled circles) and their best-fit DUSTY SEDs (solid lines). Each input spectrum is shown as a dotted line. We plot  $\log(\lambda F_\lambda)$  versus  $\log(\lambda)$ .

## 5.2. Mass-loss rate, effective temperature, and luminosity

Our data, as presented in Table 3, can be used to obtain observational constraints on the dependence of mass-loss rate on effective temperature and luminosity for the first time. We assumed that the relationship should be of the form:  $\dot{M} \propto T^\alpha L^\beta$ . Adopting a factor of two uncertainty for each true mass-loss rate, a chi-squared minimization yields the power-law exponents:

$$\alpha = -8.80_{-0.24}^{+0.96} \quad \beta = +1.74_{-0.24}^{+0.16} \quad (7)$$

Theoretical studies of mass-loss for C-rich long-period variables (not yet extended to O-rich or M-type variables) suggests that their mass-loss rates are mainly governed by stellar photospheric temperature, followed by mass and luminosity, and are relatively independent of amplitude of variation, C over-abundance, and pulsational period (Arndt, Fleischer & Sedlmayr 1997). They



obtain

$$\dot{M} \propto T_{\text{eff}}^{-8.26} L^{1.53}. \quad (8)$$

which is in good agreement with our observations.

### 5.3. Dust-based mass-loss rates from 15 $\mu\text{m}$ photometry

Table 3 includes the excess of 15  $\mu\text{m}$  flux based on a Rayleigh-Jeans extrapolation of the 7  $\mu\text{m}$  flux ( $x[15]$  in mJy) for each star. We can calibrate this quantity in terms of the true mass-loss rate, as given by the DUSTY models, yielding

$$\log \dot{M} = 0.78(\pm 0.08) \cdot \log(x[15]) - 7.88(\pm 0.11), \quad (9)$$

with a s.d. = 0.30 dex. This formula should be valid for SRs having observed 15  $\mu\text{m}$  excesses from 3 to 130 mJy, giving mass-loss rates from  $1 \times 10^{-8}$  to  $5 \times 10^{-7} M_{\odot} \text{ yr}^{-1}$ .

As previously explained, determination of the 15  $\mu\text{m}$  continuum by Rayleigh-Jeans extrapolation of the 7  $\mu\text{m}$  flux will not be correct for objects whose dust shells become optically thick at shorter wavelengths than is usually the case for SRs. Thus, in particular, we do not expect long-period Miras to follow the empirical relationship given.

It is instructive to compare our values with those given by the Jura (1987) formula for the mass-loss from an AGB star:

$$\dot{M} = 1.7 \times 10^{-7} \left( \frac{150}{\chi_{60}} \right) v_{15} R_{\text{kpc}}^2 L_4^{-1/2} F_{\nu,60} \lambda_{10}^{1/2} M_{\odot} \text{ yr}^{-1}, \quad (10)$$

where  $v_{15}$  is the gas outflow velocity in units of  $15 \text{ km s}^{-1}$ , determined from CO observations,  $R$  is the distance to the star in kpc,  $L_4$  is the stellar luminosity in units of  $10^4 L_{\odot}$ ,  $F_{\nu,60}$  is the flux from the object at 60  $\mu\text{m}$  in Jy,  $\lambda_{10}$  is the mean wavelength of light emerging from the star in units of 10  $\mu\text{m}$ , and  $\chi_{60}$  is the dust absorption coefficient in units of  $\text{cm}^2 \text{ g}^{-1}$ . We adopt  $R \sim 8.7$  kpc,  $L_4 = 0.3$ , ( $M_{\text{bol}} = -4.04$ ) and  $\lambda_{10} = 0.1$  from the bolometric magnitude of a 200-day Mira (Glass et al. 1995). To relate the given 15  $\mu\text{m}$  flux to the 60  $\mu\text{m}$  flux required, we take the relation by Jura (1986), intended for carbon stars (but see also the values of  $Q_{\text{abs}}$  for astronomical silicate grains; Draine & Lee 1984), namely  $F_{\nu} \propto \nu^{1.54}$ . As noted above, our DUSTY models employ  $\chi_{60} = 70 \text{ cm}^2 \text{ g}^{-1}$ . Finally, we adopt the mean expansion velocity of those listed in Table 3, or  $16 \text{ km s}^{-1}$ ; this compares to  $8 \text{ km sec}^{-1}$ , the average value determined for semi-regular variables by Kerschbaum, Olofsson & Hron (1996). If the excess 15  $\mu\text{m}$  flux is 100 mJy, we obtain  $\dot{M} = 2 \times 10^{-7} M_{\odot} \text{ yr}^{-1}$ . This is within a factor of two of the mass-loss rate expected from our calibration,  $4 \times 10^{-7} M_{\odot} \text{ yr}^{-1}$  for a similar 15  $\mu\text{m}$  flux excess. Thus our mass-loss rate calibration and Jura's well-known calibration yield similar results.

#### 5.4. Mass-loss rate and Pulsation Periods

The part of the  $15\mu\text{m}$  flux emitted by dust ( $x[15]$ ) for the whole sample of SRs has been estimated by subtracting the photospheric flux which was taken to be a Rayleigh-Jeans tail fitted to the  $7\mu\text{m}$  measurements. The latter were assumed to be completely free of dust emission. Figure 8 shows this quantity  $x[15]$  as a function of log period. Although the same procedure has been applied to the Miras, which are also included in Fig. 8, it becomes unreliable with increasing period because the assumption that the  $7\mu\text{m}$  flux is free of a dust component progressively ceases to be valid.

It is evident from Fig. 8 that the mass-loss rates of the longer-period SRs overlap those of the short-period Miras and clearly do not depend on the presence of large-amplitude pulsation. The lack of measurable mass-loss for stars with periods  $P < 60$  days accords with the finding of Kerschbaum, Olofsson & Hron (1996, see below) that CO radio emission is not detected for  $0 < P < 75$  days. Similarly, though stars with periods in the range  $75 < P < 175$  days may show dust emission, as they may also show CO emission, this does not constitute a *sufficient* condition.

#### 5.5. CO-based information

As noted above, the period-dependent behavior of the quantity  $x[15]$  for SRs in the Galactic bulge is consistent with that of CO detections for SRs found in the solar neighborhood. It is therefore of interest to briefly recall the CO-based information.

Kahane & Jura (1994) found CO emission from 11 SRs with measured periods (typically 100-160 days) and brighter than  $K = 0$ . They determined mass-loss rates of  $1\text{--}1.5 \times 10^{-7} M_{\odot} \text{yr}^{-1}$ , which they compared to calculations based on the dust mass-loss rates derived from IRAS  $60\mu$  fluxes. Similar dust-to-gas ratios, CO line ratios, outflow velocities and mass-loss rates were found as for Miras with  $300 \leq P \leq 400$  days period, leading to the speculation that this group of SRs were overtone pulsators corresponding to the Miras which pulsate in the fundamental mode. Kerschbaum, Olofsson and Hron (1996) extended their sample to another group of SRs and SRbs, selected on the basis of their  $60\mu\text{m}$  fluxes. The Kerschbaum & Hron (1992) blue SRVs were not detected, whereas the red ones and the Miras had a 50% detection rate. Those with periods below 75 days were not seen, nor were those with  $175 \leq P \leq 325$  days. Those with  $75 \leq P \leq 175$  had a high detection rate. A CO study by Young (1995) of nearby Miras with optically thin dust shells showed that only stars of type later than M5.5 could be detected, the rate becoming 100% only for M7 and later types. The mass-loss rate was found to be correlated with far-IR luminosity but not color, and also with CO outflow velocity. Similar mass-loss rates were found for M6.5–M8 types (comparable to the rates for semiregular variables found by other workers).

### 5.6. Mass-loss rates as a function of luminosity only

We have seen that mass-loss in SRs can be expressed as a function of  $T$  and  $L$ . High luminosities and long periods in LPVs are associated with low temperatures, which are not independent variables but are connected by evolutionary tracks.

Figure 9 shows  $M_{\text{bol}}$  plotted against the mass-loss rates from Table 3 of our work together with those derived for dust-enshrouded O- and C-rich AGB stars in the LMC by van Loon et al. (1999). There is a striking continuity between the rates exhibited by the low-luminosity semi-regular variables and those found amongst the extreme AGB-tip variables, both C-type and M-type, in the LMC, in spite of the differences in metallicities between the samples. We have derived a linear fit between  $\log \dot{M}$  and  $M_{\text{bol}}$ . Because the distribution of errors between these quantities is uncertain, we have solved first assuming that all the errors are in  $M_{\text{bol}}$  and second assuming that they are in  $\dot{M}$ . Both fits are shown and the average slope is given by the solid line, whose form is

$$\dot{M} \propto -1.09M_{\text{bol}}, \quad (11)$$

i.e., we find that

$$\dot{M} \propto L^{2.7}, \quad (12)$$

in the range  $10^{-8} < \dot{M} < 10^{-4} M_{\odot} \text{ yr}^{-1}$ .

## 6. Conclusions

1. Almost all non-Miras in our sample detected in the four MACHO and ISO colors show semi-regular variability.
2. The SRs outnumber Miras by 20:1 in our sample.
3. We see no preferred periods in 10-200 day range, but a gap exists between the distributions of SRs and Miras which may be explicable in terms of pulsation modes.
4. The Galactic bulge SRs possess a  $P - L$  distribution similar to that of the solar neighbourhood SRs observed by Hipparcos. They can probably be regarded as lying on a series of  $P - L$  relations with slopes equal to that observed in globular clusters, but with luminosity levels appropriate to higher metallicities and initial masses.
5. The amplitudes of the SRs increase with period, reaching about 0.3 mag at 100 days.
6. Mass loss depends on luminosity and period, but does not require large Mira-like amplitudes, even though the mass-loss levels reach those of the shorter-period Miras.
7. A minimum period of about 70d is required for, but does not guarantee, detectable mass loss, in agreement with conclusions based on CO observations.

8. The mass-loss rate for semi-regular variables depends on temperature and luminosity approximately according to  $\dot{M} \propto T^{-8.8} L^{1.7}$ .

9. The observed mass-loss rates in SRs range from  $1 \times 10^{-8} M_{\odot} \text{ yr}^{-1}$  to  $5 \times 10^{-7} M_{\odot} \text{ yr}^{-1}$ .

10. Taking into account the work of van Loon et al. (1999) concerning extreme mass-losing AGB stars in the LMC, we find the general result that  $\dot{M} \propto L^{2.7}$  in the range  $10^{-8} < \dot{M} < 10^{-4} M_{\odot} \text{ yr}^{-1}$ .

Note that in this work we have discussed only those stars which were detected in both MACHO and both ISOGAL bands. A preliminary examination of the light curves of the stars seen by ISOGAL only at  $7 \mu\text{m}$  indicates that most of them are also SRs, but presumably with mass-loss rates too low for  $15 \mu\text{m}$  detection.

D.R.A. acknowledges support of this work from a NASA grant administered by the American Astronomical Society. D.R.A. also thanks the South Africa Astronomical Observatory for his appointment to the Visiting Astronomer Program, and acknowledges their financial support of his visit.

I.S.G. thanks the Institute of Astronomy, University of Cambridge, and the Institut d’Astrophysique, Paris, for their hospitality and support during part of this work, under PPARC and CNRS grants, respectively.

We thank M. Groenwegen for useful comments on an early version of this paper.

The MACHO Collaboration thanks the skilled support by the technical staff at MSSSO. Work at LLNL was performed under the auspices of the U.S. Department of Energy by the University of California Lawrence Livermore National Laboratory under contract No. W7405-ENG-48. Work at CfPA was supported by NSF AST-8809616 and AST-9120005. Work at MSSSO was supported by the Australian Dept. of Industry, Technology and Regional Development. W.J.S. thanks PPARC Advanced Fellowship, K.G. thanks DOE OJI, Sloan, and Cottrell awards, C.W.S. thanks Sloan and Seaver Foundations. D.M. is supported by Fondecyt 1990440.

## REFERENCES

- Alcock, C. et al. 1999, PASP, 111, 1539
- Alcock, C. et al. 2000, AJ, 119, 2194
- Alves, D. et al. 1998, proc. of IAU JD 24, “Pulsating Stars: Recent Developments in Theory and Observation”, eds. D. Sasselov & M. Takeuti (Tokyo: Universal Academy Press)
- Arndt, T.U., Fleischer, A.J., & Sedlmayr, E. 1997, A&A, 327, 614
- Bedding, T.R. & Zijlstra, A.A. 1998, ApJ, 506, L47
- Bessell, M.S., Brett, J.M., Scholz, M., & Wood, P.R. 1989, A&A, 213, 209
- Bessell, M.S., Castelli, F., & Plez, B. 1998, A&A, 333, 231
- Blanco, V.M. 1986, AJ, 91, 290
- Blanco, V.M., McCarthy, M.F., & Blanco, B. 1984, AJ, 89, 636
- Bowen, G.H. 1988, ApJ, 329, 299
- Bowen, G.H. & Willson, L.A. 1991, ApJ, 329, L53
- Cesarsky, C.J. et al. 1996, A&A, 315, L32
- de Gioia-Eastwood, K., Hackwell, J.A., Grasdalen, G.L., & Gehrz, R.D. 1981, ApJ, 245, L53
- Draine, B.T. & Lee, H.M. 1984, ApJ, 285, 89
- Fleischer, A.J., Gauger, A., & Sedlmayr, E. 1992, A&A, 266, 321
- Frogel, J.A. & Whitford, A.E. 1987, ApJ, 320, 199
- Gail, H.-P., Cuntz, M., & Ulmschneider, P. 1990, A&A, 234, 359
- Gilman, R.C. 1972, ApJ, 178 423
- Glass, I.S., Alves, D., & the ISOGAL & MACHO teams, 2000, in *ISO Surveys of a Dusty Universe*, D. Lemke, M. Stickel, & K. Wilke (eds.), Lecture Notes in Physics Series, Springer-Verlag, in press
- Glass, I.S., Catchpole, R.M., Feast, M.W., Whitelock, P.A., & Reid, I.N., 1987, in *Late Stages of Stellar Evolution*, S. Kwok & S.R. Pottasch (eds.), Reidel Dordrecht
- Glass, I.S., Whitelock, P.A., Catchpole, R.M., & Feast, M.W. 1995, MNRAS, 273, 383
- Glass, I.S., Ganesh, S., Alard, C., Blommaert, J.A.D.L., Gilmore, G., Lloyd Evans, T., Omont, A., Schultheis, M., & Simon, G. 1999, MNRAS, 308, 127
- Habing, H.J., 1996, A&A Review, 7, 97
- Hinkle, K.H., Lebzelter, T., & Scharlach, W.W.G. 1997, AJ, 114, 2686
- Hoyle, F. & Wickramasinghe, N.C. 1962, MNRAS, 124, 417
- Iben, I. & Renzini, A. 1983 ARA&A, 21, 271

- Ivečić, Z., Nenkova, M., & Elitzur, M. 1999, *User Manual for Dusty*, preprint (astro-ph/9910475)
- Jura, M., 1986, ApJ, 303, 327
- Jura, M., 1987, ApJ, 313, 743
- Jura, M. & Kleinman, S. 1992, ApJS, 83, 329
- Kahane, C. & Jura, M. 1994, A&A, 290, 183
- Kerschbaum, F. & Hron, J. 1992, A&A, 263, 97
- Kerschbaum, F., Olofsson, H., & Hron, J. 1996, A&A, 311, 273
- Koen, C. & Laney, C.D. 2000, MNRAS, 311, 638
- Kwok, S. 1975, ApJ, 198, 583
- Lafon, J.P.-J. & Berruyer, N. 1991, A&AR, 2, 249
- Lejeune, T., Cuisinier, F., & Buser R. 1997, A&AS, 125, 229
- Lloyd Evans, T. 1976, MNRAS, 174, 169
- Mathis J.S., Rumpl W., & Nordsieck, K.H., 1977, ApJ, 217, 425
- Menessier et al., 2000, in preparation
- Minniti, D. et al 1998 proc. of IAU JD 24, “Pulsating Stars: Recent Developments in Theory and Observation”, eds. D. Sasselov & M. Takeuti (Tokyo: Universal Academy Press)
- Morris, M. 1987, PASP, 99, 1115
- Omont, A. et al. 1999, A&A, 348, 755
- Omont, A. et al. & the ISOGAL Collaboration, 2000, in *ISO Surveys of a Dusty Universe*, D. Lemke, M. Stickel, & K. Wilke (eds.), Lecture Notes in Physics Series, Springer-Verlag, in press
- Payne-Gaposchkin, C. 1951, in *Astrophysics*, J.A. Hynek (ed.), McGraw-Hill, New York
- Reid, M.J. & Menten, K.M. 1997, ApJ, 476, 327
- van Loon, J. Th., Groenewegen, M.A.T., de Koter, A., Trams, N.R., Waters, L.B.F.M., Zijlstra, A.A., Whitelock, P.A., & Loup, C., 1999, A&A, 351, 559
- Vassiliadis, E. & Wood, P. 1993, ApJ, 413, 641
- Whitelock, P.A. 1986, MNRAS, 219, 525
- Whitelock, P.A. et al. 1994, MNRAS, 267, 711
- Whitelock, P., Menzies, J., Feast, M., Catchpole, R., Marang, F., & Carter, B. 1995, MNRAS, 276, 219
- Willson, L.A. 1976, ApJ, 205, 172
- Willson, L.A. & Hill, S.J., 1979, ApJ, 228, 854
- Winters, J.M., Fleischer, A.J., Gauger, A., & Sedlmayr, E. 1994, A&A, 288, 255

Wood, P.R. 1979, ApJ, 227, 220

Wood, P.R. 2000, Publ. Astr. Soc. Austr., 18, 18

Wood, P.R. et al. 1999, proc. of IAU Symposium 191 “Asymptotic Giant Branch Stars”, p. 151

Wood, P.R. & Sebo, K.M., 1996, MNRAS, 282, 958

Young, K. 1995, ApJ, 445, 872

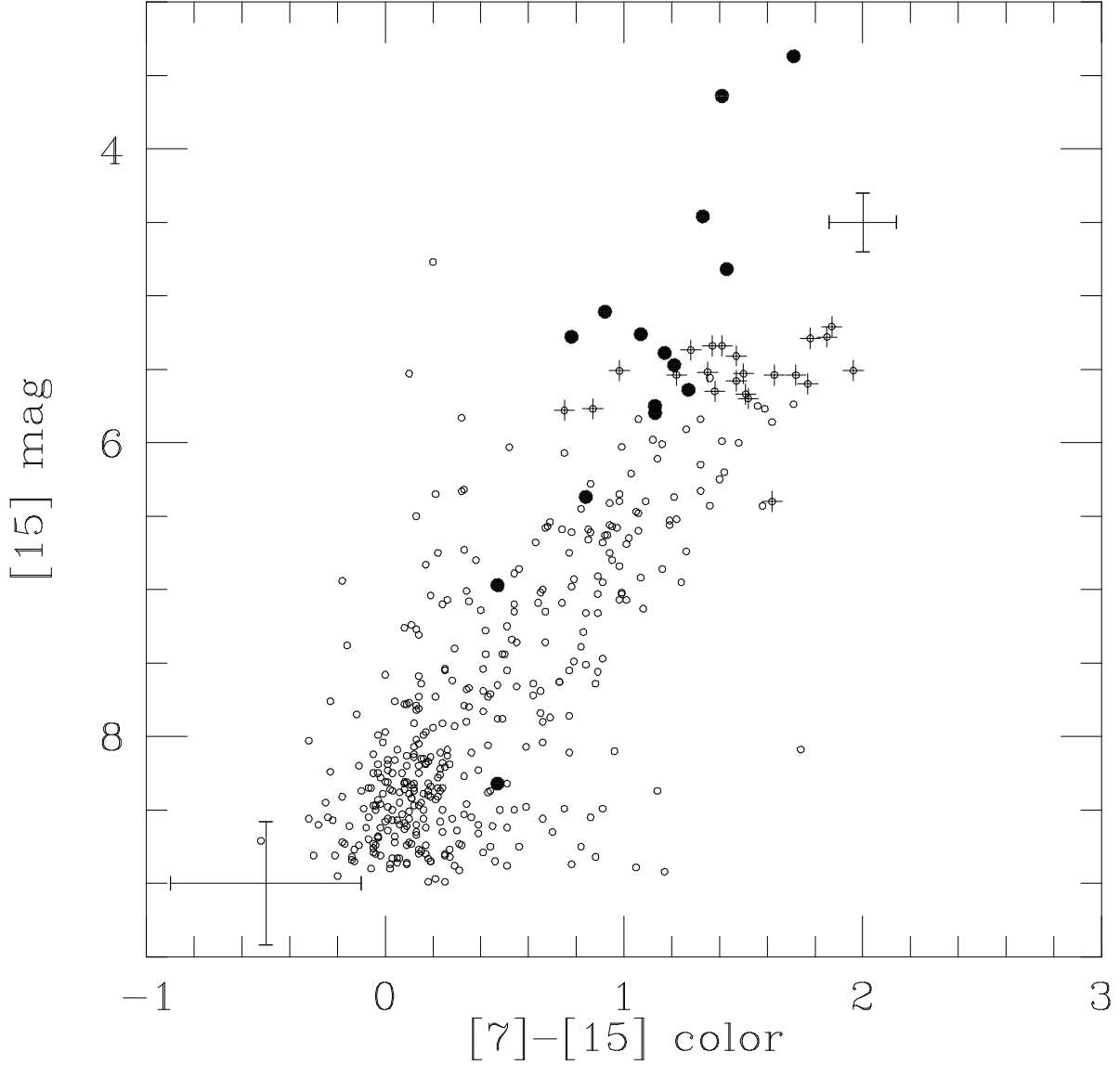


Fig. 1.— Combined ISOCAM color-magnitude diagram for the  $15 \times 15$  arcmin<sup>2</sup> fields in the NGC 6522 and Sgr I windows. Note the characteristic sequence of increasing  $15 \mu\text{m}$  flux, representative of mass-loss, with  $[7] - [15]$  color. The heavy dots represent Mira variables and the crosses are bright stars that were examined unsuccessfully for variability in the pre-MACHO data. The top of the red giant branch (RGB) is around  $[15] \sim 8$ . The objects brighter than this level are asymptotic-giant-branch (AGB) stars, except for a few foreground objects. Representative error bars are shown at each end of the sequence.



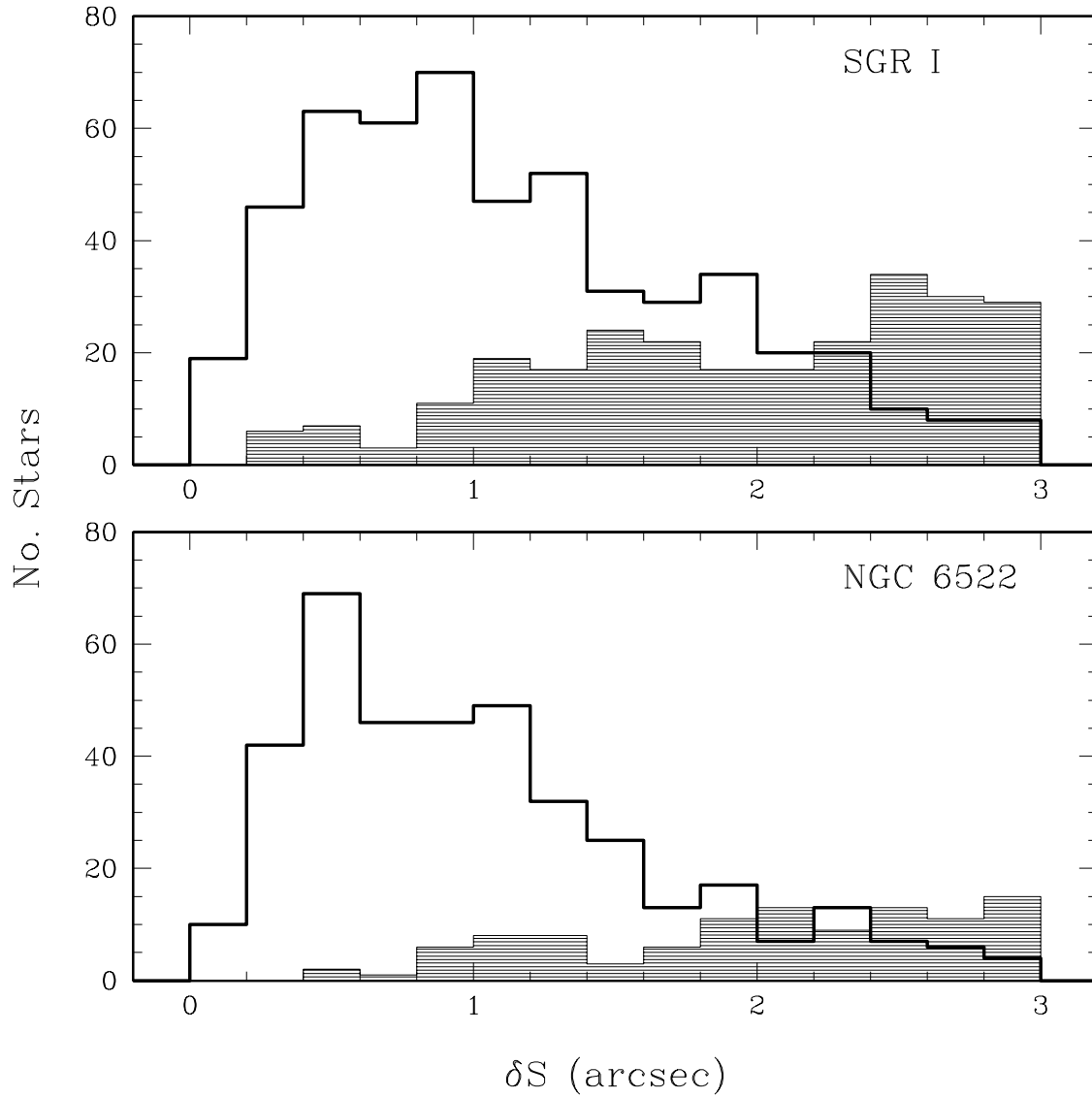


Fig. 2.— The distribution of  $\delta S$  (the angular distance between ISOGAL and MACHO source coordinates in arcseconds) for the final match lists. Example distributions of spurious matches are also shown (shaded histograms).

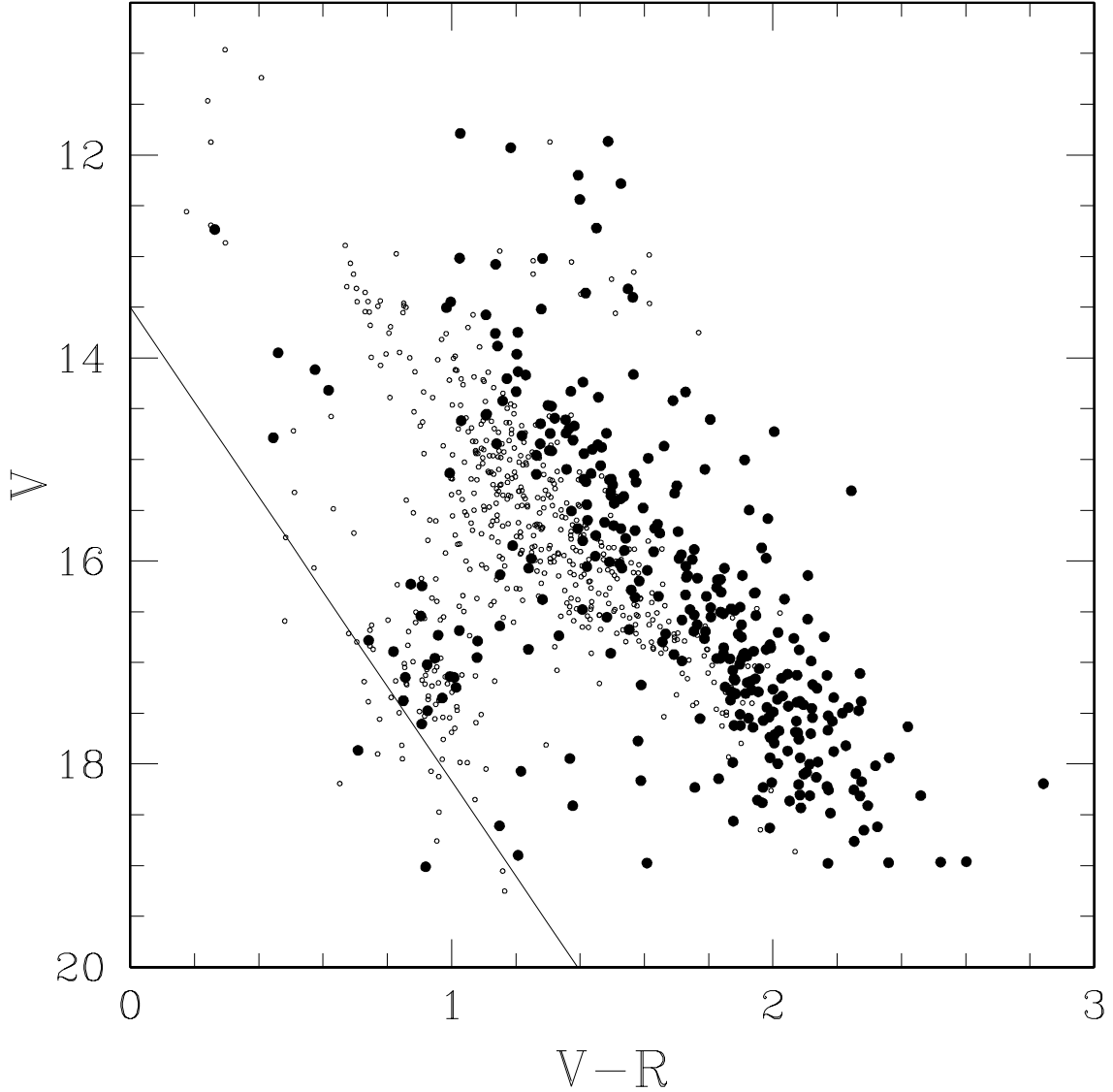


Fig. 3.— The optical CMD for MACHO+ISOGAL sources in the SGR I and NGC 6522 fields. 904 matched sources with MACHO  $V$  and  $R$  colors are shown as open circles. Sources with four colors ( $V$ ,  $R$ , [7], and [15]), are shown with bold filled circles. The  $V,(V-R)$  cut described in §3 is shown as a solid line. The four-color sources lie mostly in the reddest areas of the AGB. Some sources are foreground stars, and some are possible spurious matches (i.e., near the red clump at  $V \sim 17$ ,  $V-R \sim 0.9$ ).

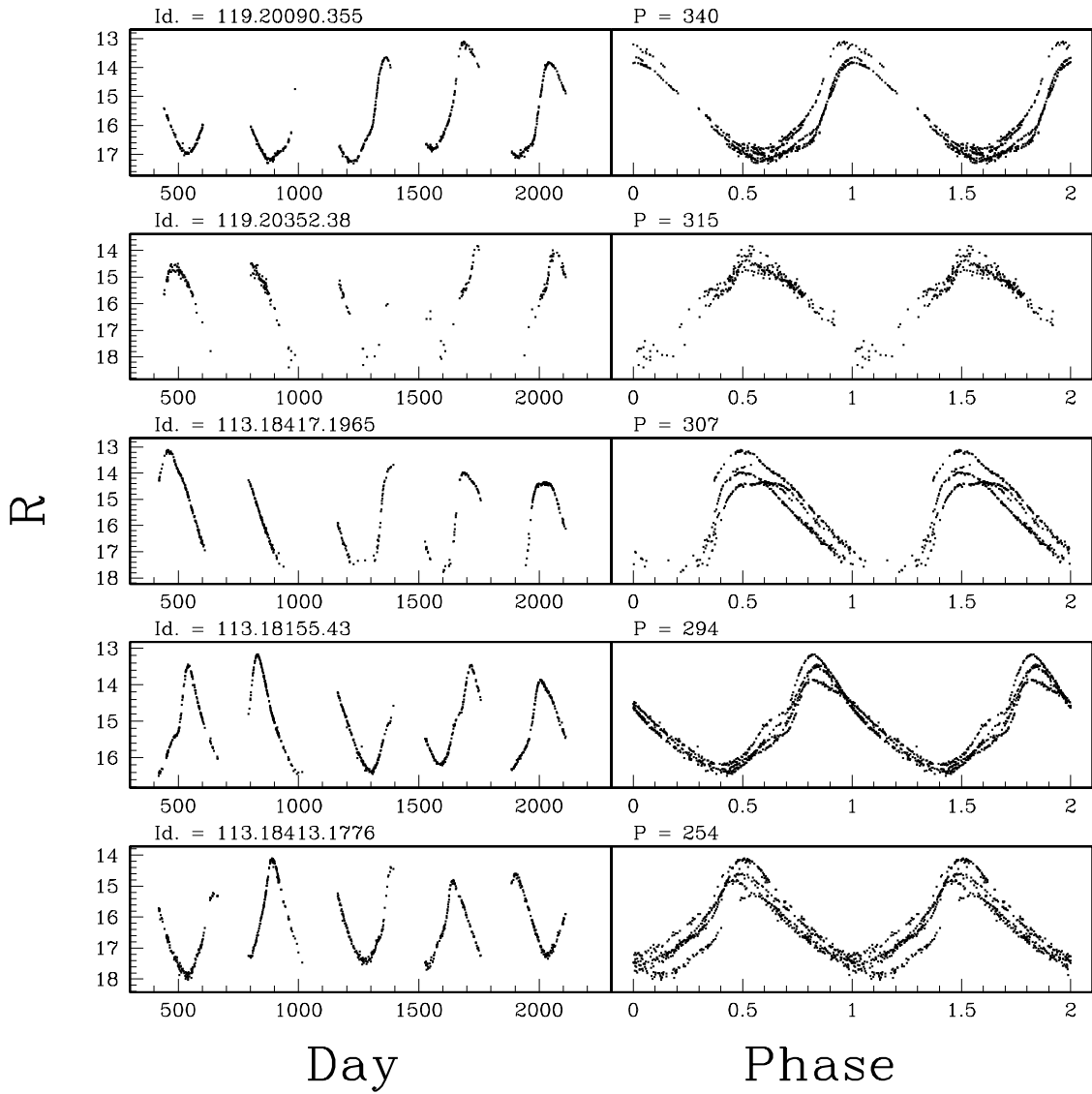


Fig. 4.— (a) Left: MACHO  $R$  light curves (mag vs. day) for five Miras. Right: Same, folded according to period (mag vs. phase).

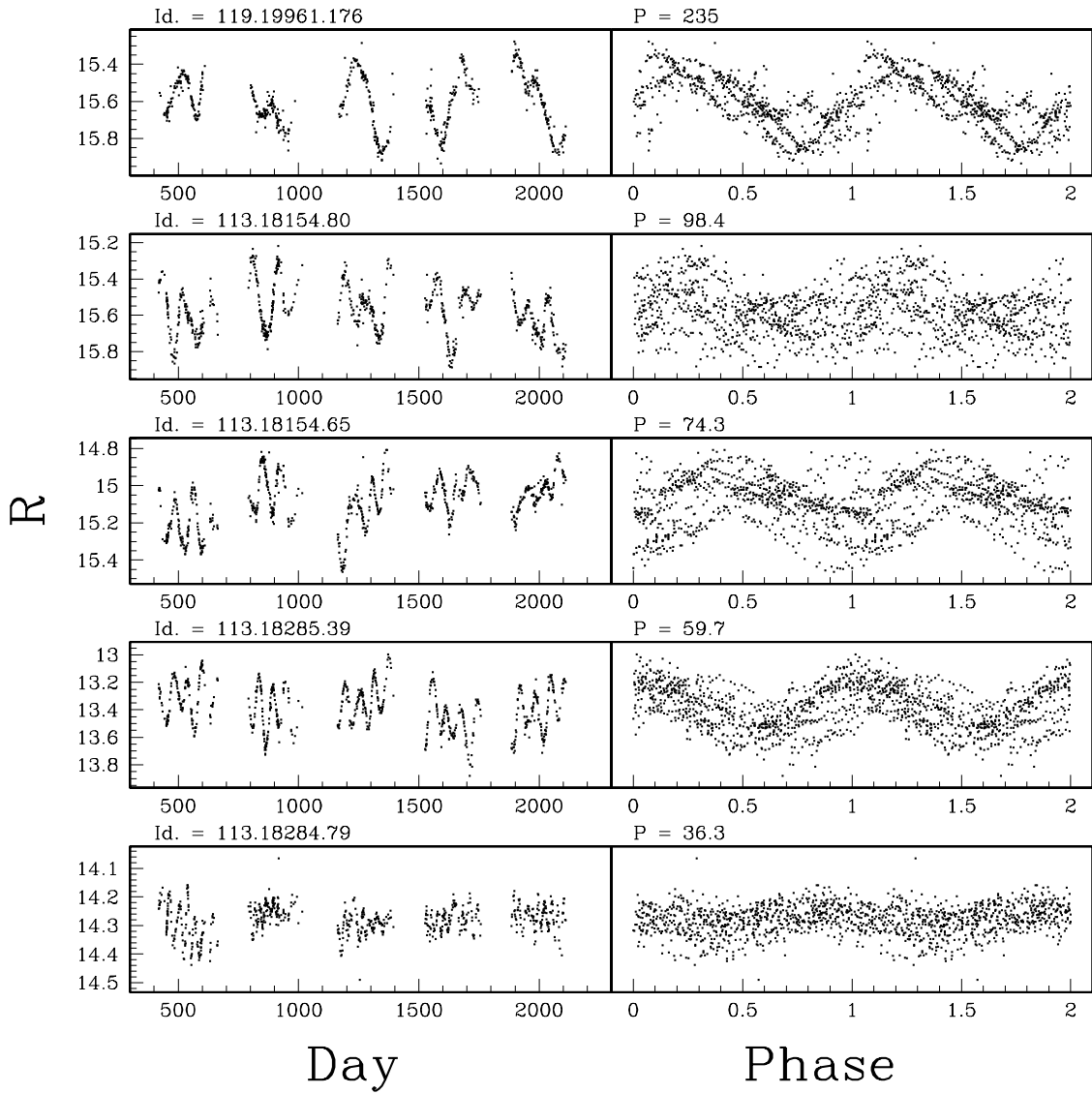


Fig. 4.— (b) Left: MACHO  $R$  light curves (mag vs. day) for five variables classified SRa. Right: Same, folded according to period (mag vs. phase).

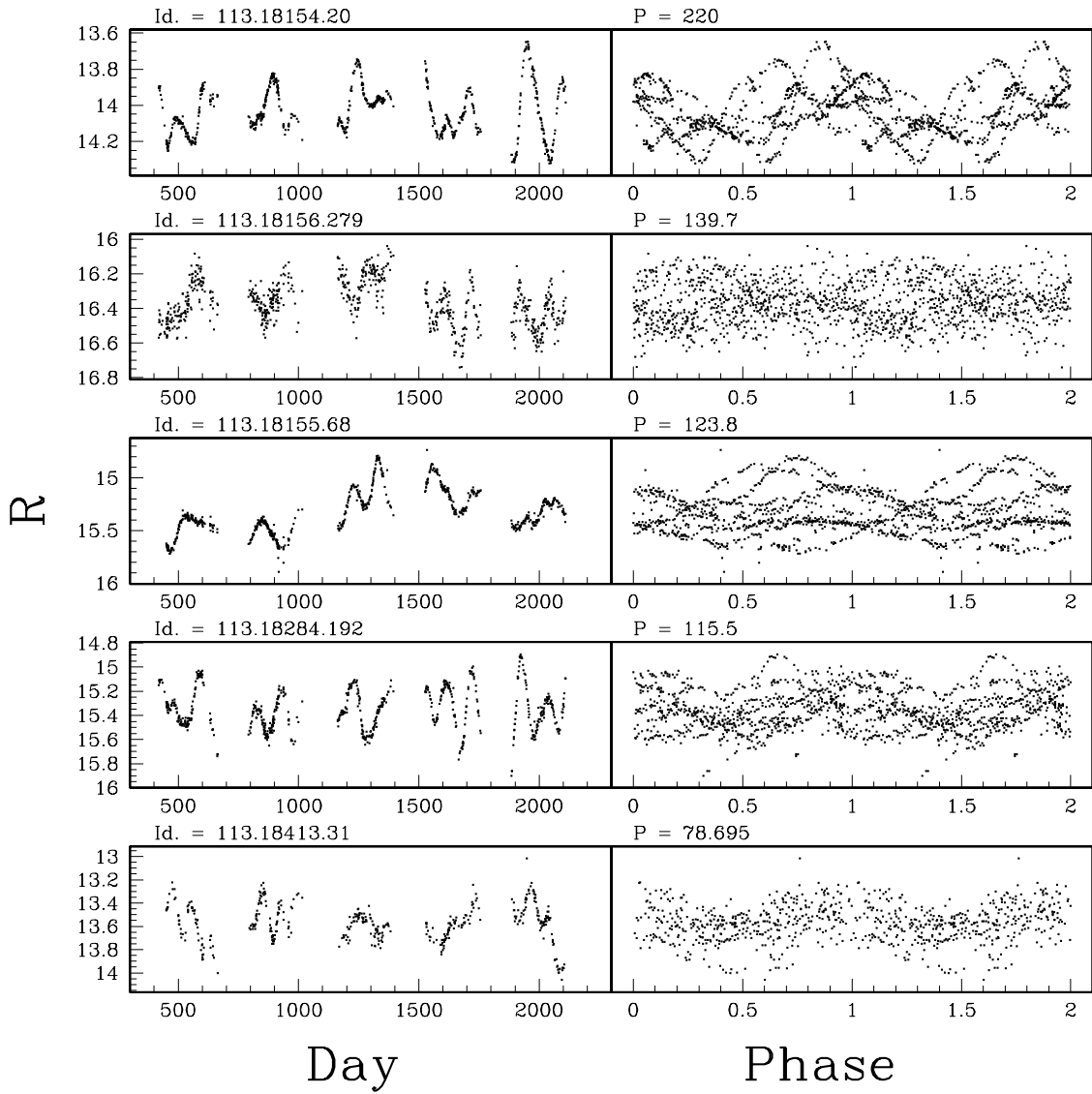


Fig. 4.— (c) Left: MACHO  $R$  light curves (mag vs. day) for five variables classified SRb. Right: same, folded according to period (mag vs. phase).

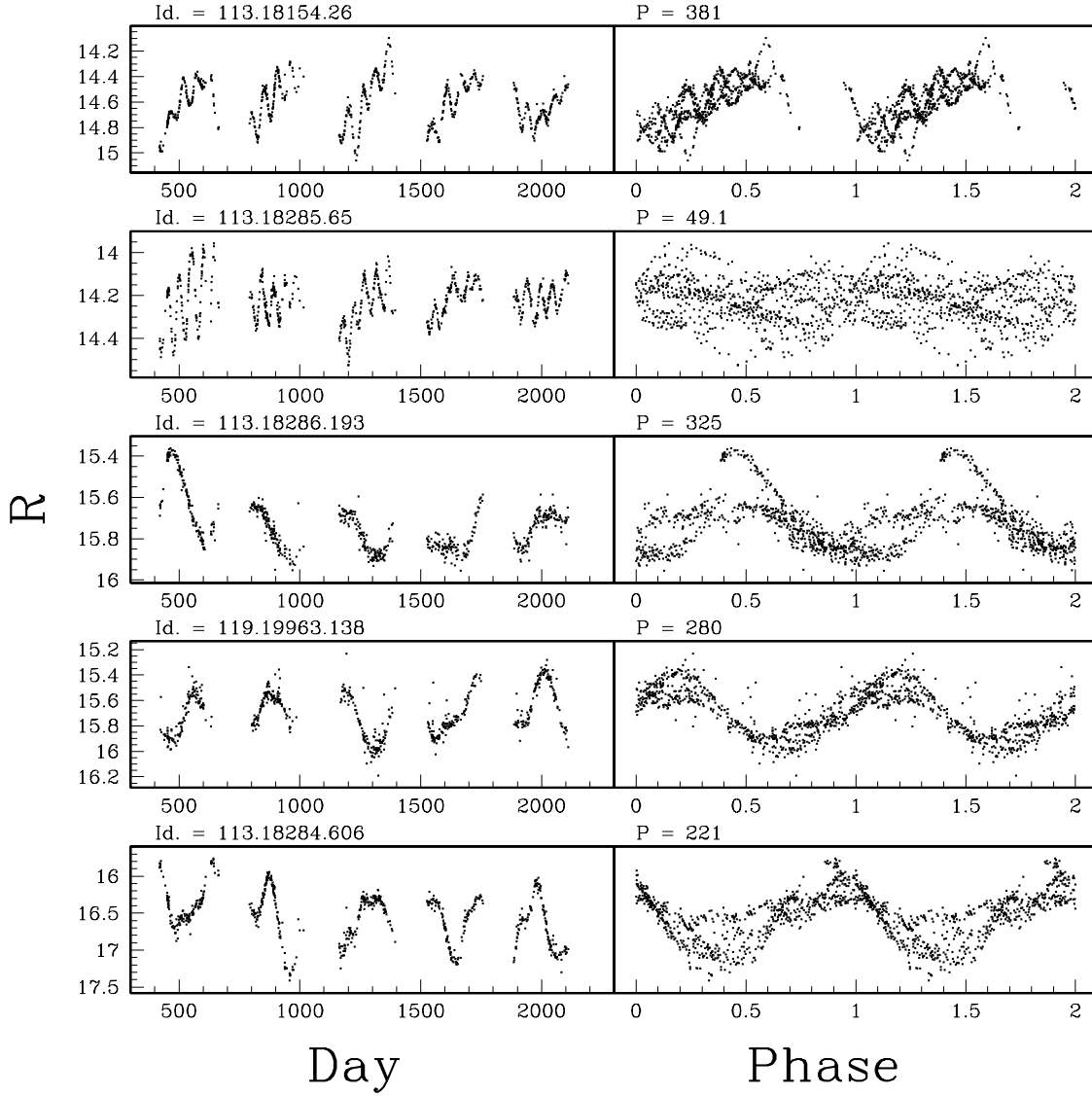


Fig. 4.— (d) Left: MACHO  $R$  light curves (mag vs. day) of two double-period variables (upper panels) and three large-amplitude SRas (bottom panels). Right: same, folded according to period shown (mag vs. phase).

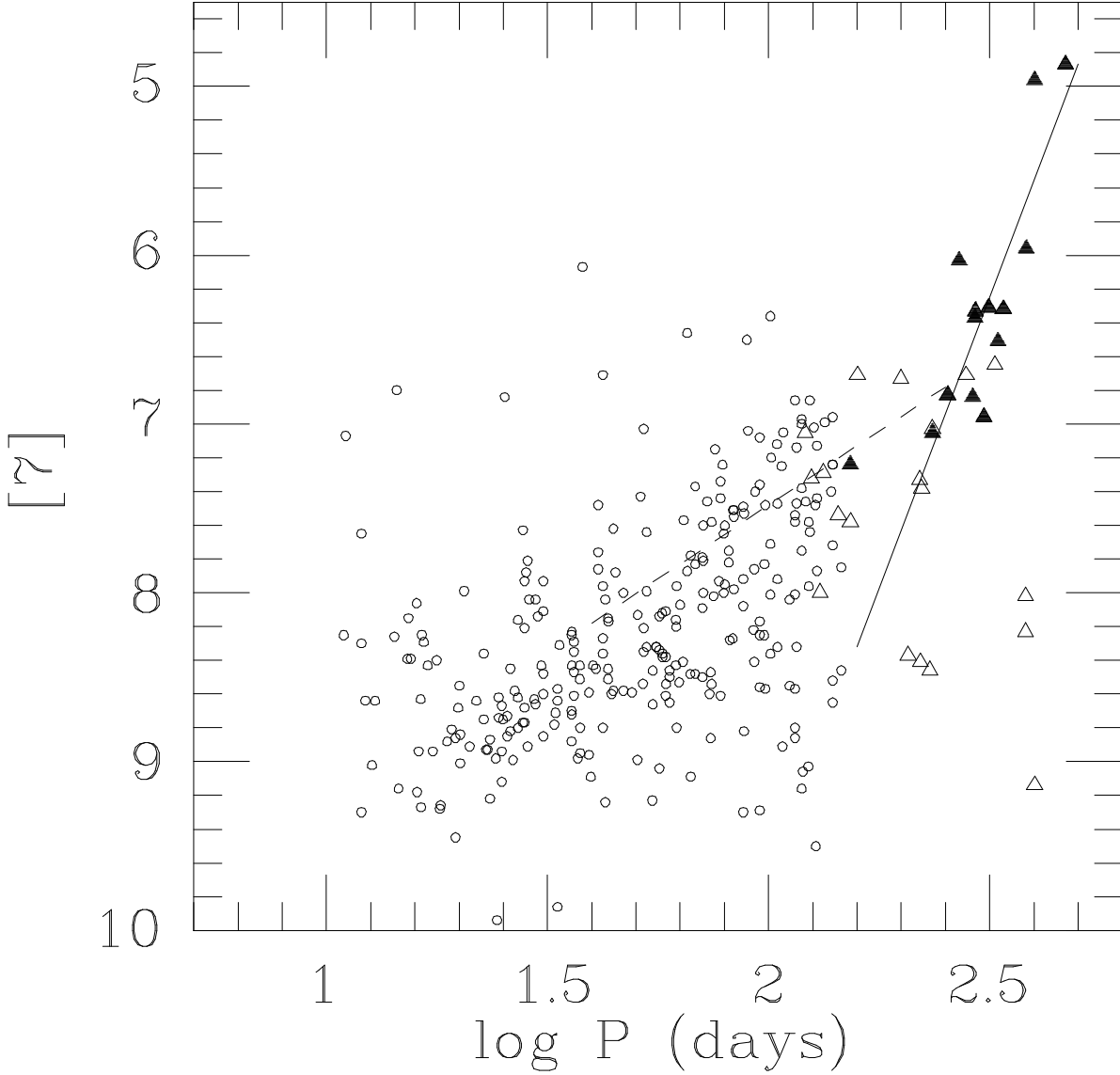


Fig. 5.— (a) The  $[7] - \log P$  diagram ( $[7]$  in mags,  $P$  in days) for cross-identified objects. The open circles are the main periods identified. Open triangles are separately identified long periods and solid triangles are Mira (large-amplitude) variables, some of which were saturated in the MACHO data. Periods for these cases were taken from Glass et al. (1995). The dashed line is an empirical period-luminosity relation derived for semiregular variables in the solar neighbourhood from Hipparcos and other data by Bedding & Zijlstra (1998). The solid line is an empirical fit to the Mira data (see text).

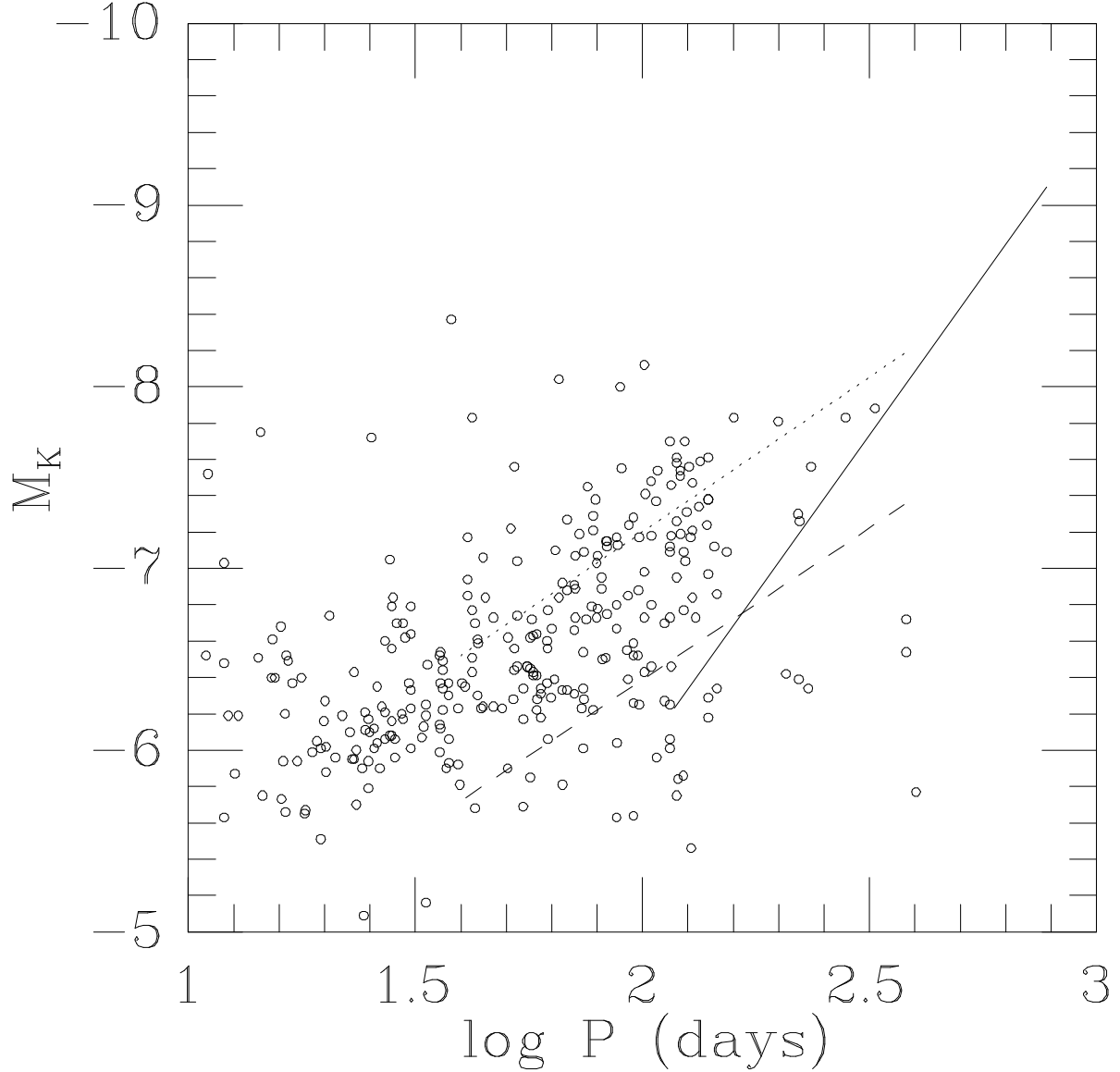


Fig. 5.— (b) Similar to Fig 5a but for  $K$ ,  $\log P$ . The solid line is a fit to Mira data for the whole Sgr I field, taken from Glass et al. (1995). (See Fig. 5c for the distribution of Miras in a similar version of this diagram.) The dotted line is from Bedding & Zijlstra (1998), representing semi-regular variables in the solar neighbourhood with known periods and distances from Hipparcos. The dashed line is the relation for globular cluster variables from Whitelock (1986) as transformed by Bedding & Zijlstra (1998).



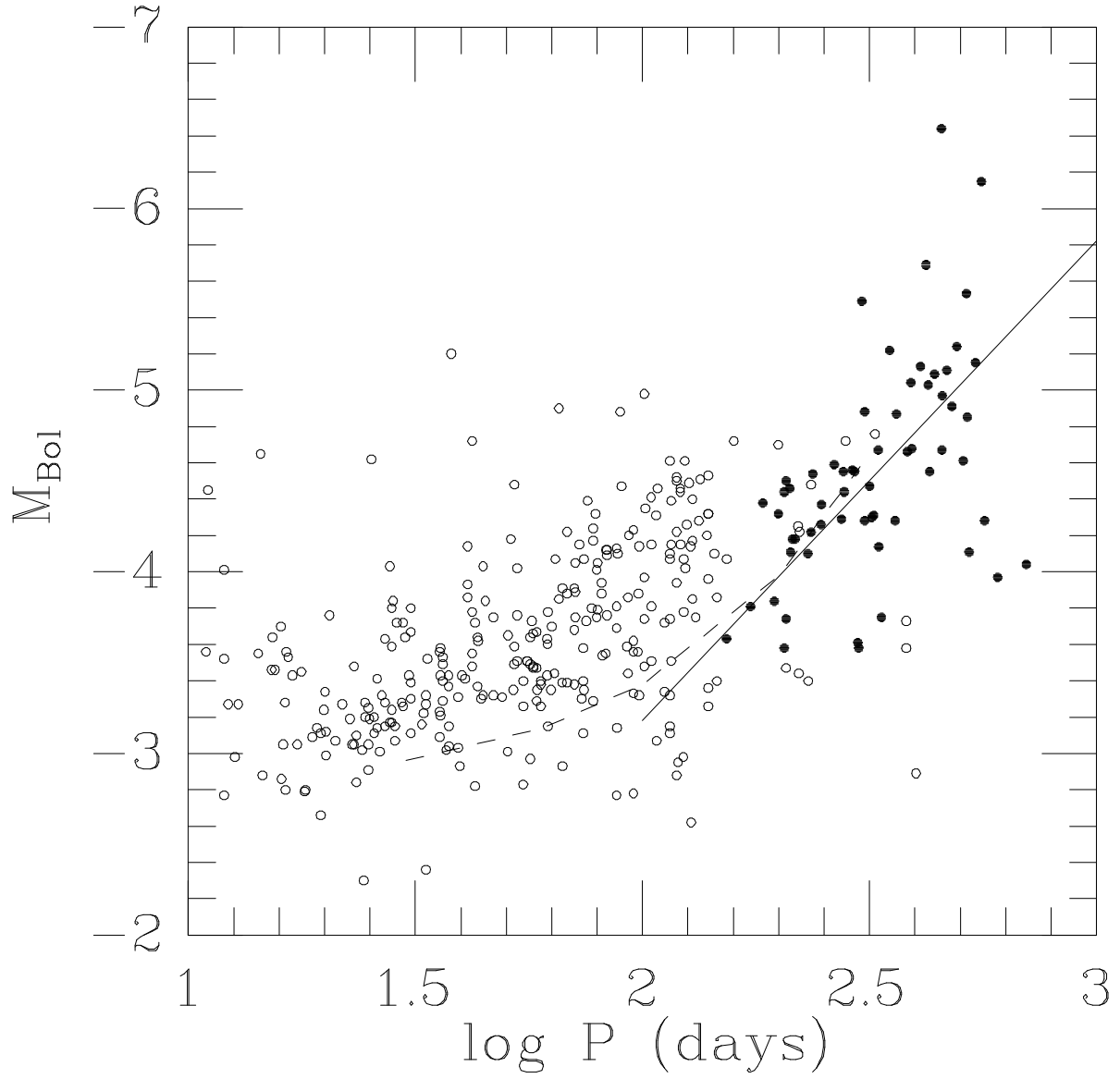


Fig. 5.— (c) Similar to Fig 5b but for  $M_{\text{bol}}$ ,  $\log P$ . Miras (dark dots) and their  $P-L$  relation (solid line) for the entire Sgr I field, have been taken from Glass et al. (1995). The dashed line is the observed relation for galactic globular clusters, taken from Whitelock (1986).

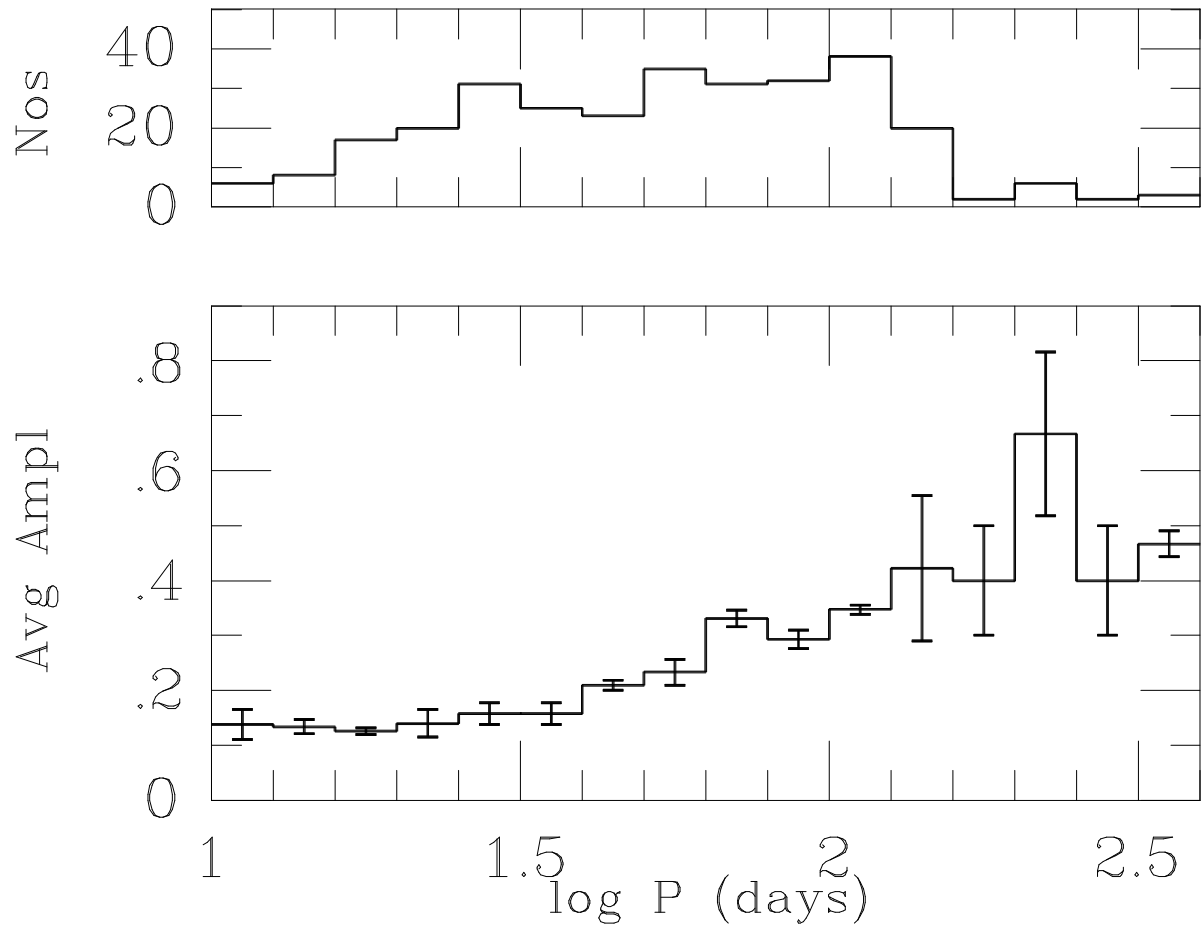


Fig. 6.— *Lower*: Histogram of mean amplitudes of all variables for  $\log(\text{period})$  groups, excluding the Miras. Standard deviations are also shown. *Upper*: Numbers of variables in each  $\log P$  box.

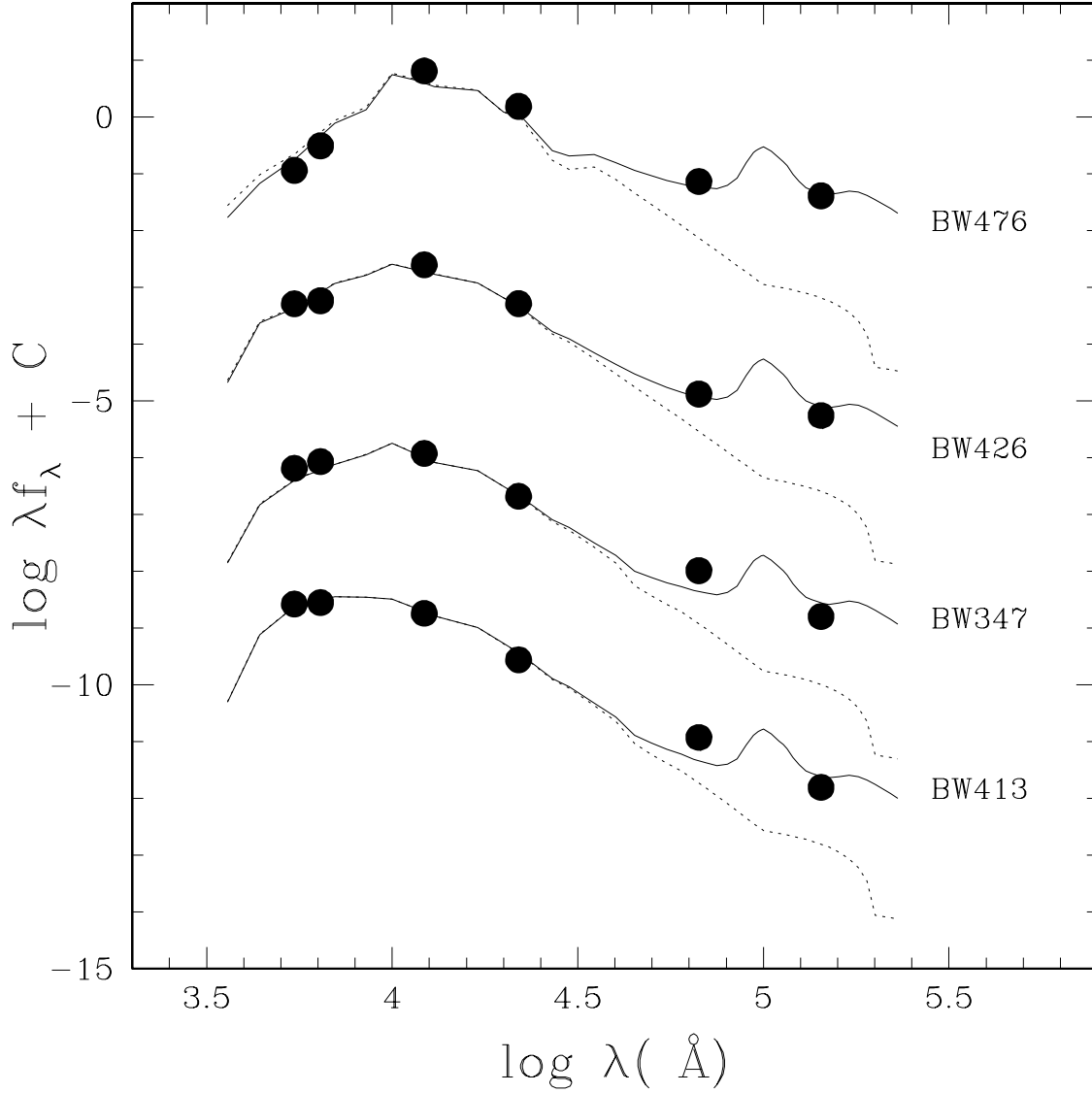


Fig. 7.— Examples of observational data for four stars (filled circles) and best-fit model spectral energy distributions (SEDs;  $\lambda F_\lambda$  in  $\text{ergs s}^{-1} \text{cm}^{-2}$  and  $\lambda$  in  $\text{\AA}$ ) including circumstellar dust (solid lines; modeled with “DUSTY”). Each input spectrum without circumstellar dust is shown as a dotted line (same units as the DUSTY model SEDs). The zero-point ( $C$ ) is arbitrary and there is a vertical offset of 3 dex between each star.

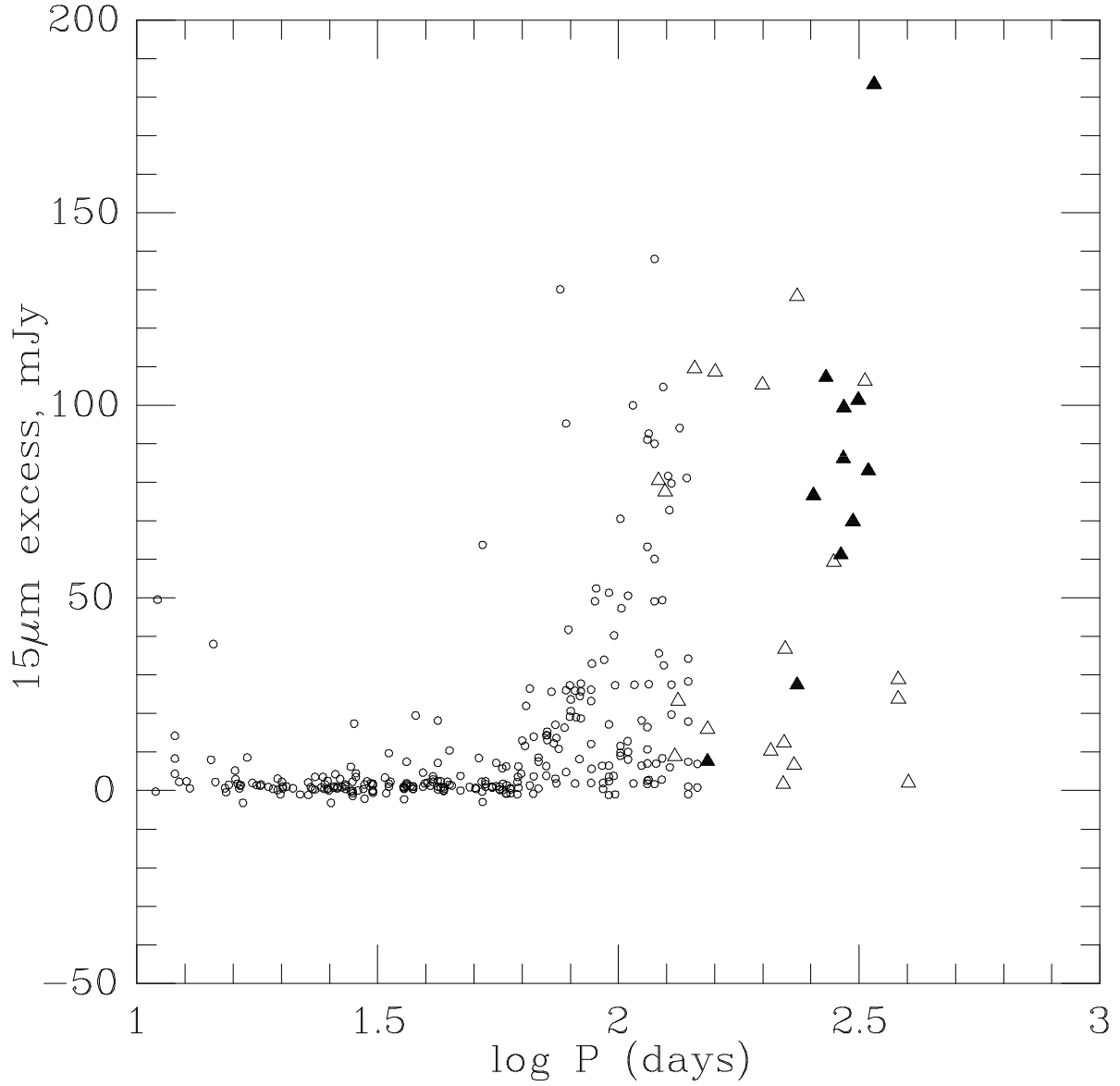


Fig. 8.— Excess  $15\mu\text{m}$  flux, an indication of mass-loss, beyond what is expected by assuming a Rayleigh-Jeans photospheric energy distribution fitted to the  $7\mu\text{m}$  fluxes, shown plotted against  $\log P$ . Symbols are as in Fig. 5a. Having a period  $P > 70$  days appears to be a necessary, but not a sufficient condition, for significant mass-loss.

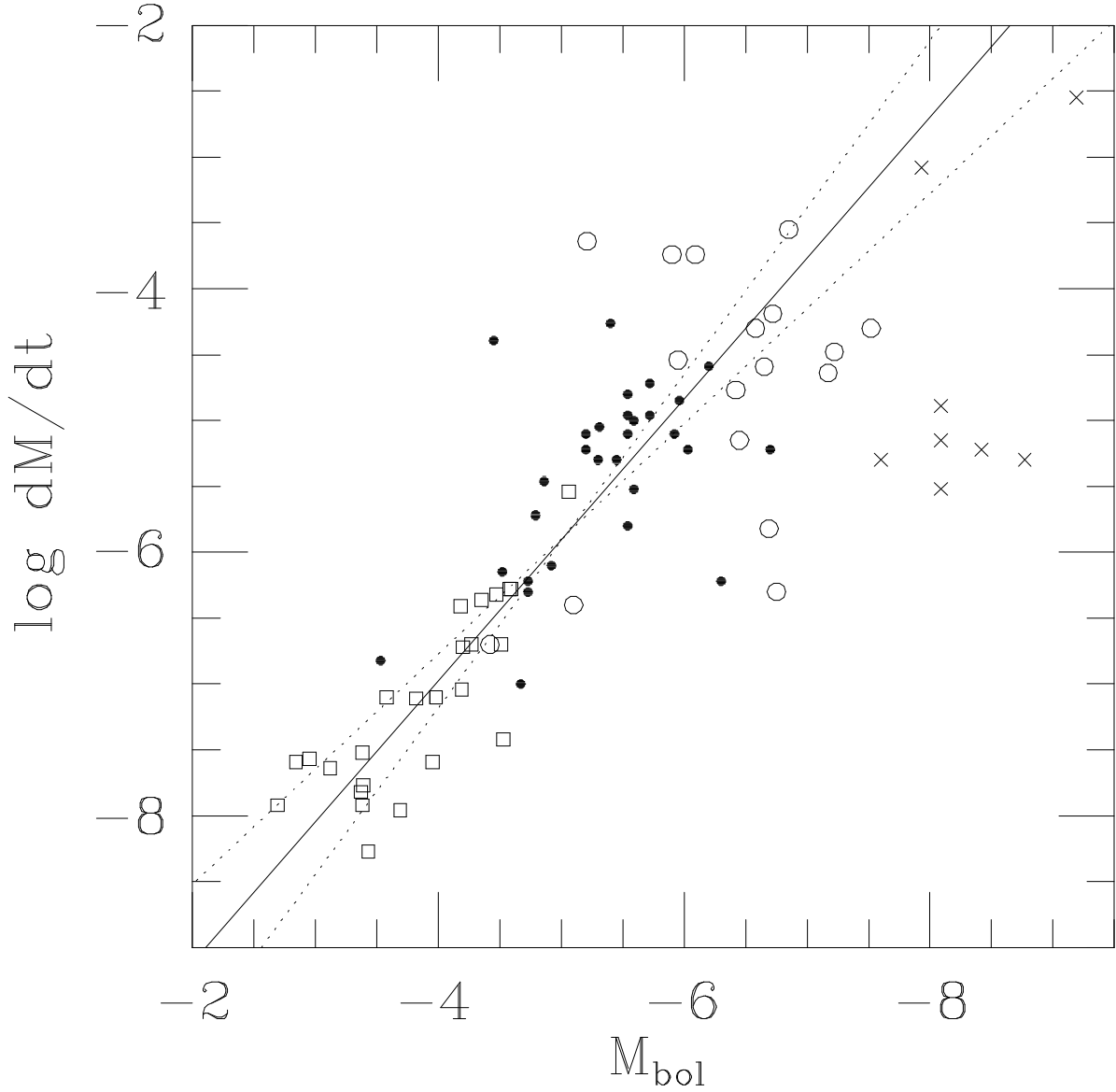


Fig. 9.—  $\dot{M}$  in units of  $M_{\odot} \text{ yr}^{-1}$  plotted against  $M_{bol}$  for our sample of Baade's Window SRs (open squares) and a sample of extreme mass-losing AGB stars in the LMC, from van Loon et al. (1999). The LMC C-type stars are shown as solid dots and M-type stars as open circles. The crosses are M supergiants. The solid line is a linear fit and the dotted lines give an indication of the errors in the slope (see text).

Table 1. Summarized Photometry of Sources

ISOGALP <sup>A</sup>	BW <sup>B</sup>	MACHO <sup>C</sup>	$V^D$	$R^D$	$J_0$	$K_0$	[7]	[15]	Amp.	$\log P^E$	notes <sup>F</sup>
J175840.5–290348	54	113 18155 17	14.92	13.47			8.61	8.07	0.2	1.891	
J175840.9–290827	57	113 18154 52	16.81	15.16			8.46	8.37	0.2	1.738	
J175841.8–290352	61	113 18155 68	17.49	15.38			6.86	5.41	0.3	2.093	
J175842.1–290650	65	113 18155 18	15.90	13.92			7.12	6.73	0.25	2.019	
J175842.4–290515	67	113 18155 251	19.06	16.65			8.04	7.07	0.4	2.048	
J175842.6–290240	68	113 18156 31	15.72	14.01			7.93	7.82	0.15	1.490	
J175842.6–291029	69	113 18154 179	18.30	16.10			7.44	6.59	0.3	1.891	
J175842.7–290340	70	113 18156 252	18.69	16.31			8.59	8.07	0.25	1.594	
J175842.9–290845	72	113 18154 65	17.25	15.11			7.58	7.00	0.3	1.871	
J175843.4–291012	74	113 18154 51	17.09	15.21			8.62	8.56	0.1	1.433	
J175843.9–290325	77	113 18156 21	14.87	13.41			8.58	8.59	0.2	1.672	
J175843.9–290712	78	113 18155 43	17.65	15.69			6.33	5.28	4.0	2.468:	Mira
J175844.6–290234	82	113 18156 38	15.68	14.05			8.55	8.28	0.12	1.301	
J175845.6–290357	87	113 18155 118	17.64	15.75			8.29	8.17	0.15	1.560	
J175845.9–290326	88	113 18156 48	16.17	14.43			8.80	8.64	0.12	1.574	
J175846.0–291033	89	113 18154 84	17.32	15.43			8.95	8.87	0.1	1.574	
J175846.0–290748	90	113 18154 108	17.68	15.65			8.67	8.61	0.15	1.396	
J175846.2–290310	93	113 18156 75	17.15	15.08			8.14	8.12	0.35	1.753	
J175846.9–290722	99	113 18155 462	18.08	16.87			8.11	7.96	0.1	1.490	
J175846.9–290332	100	113 18156 76	16.99	15.10			8.60	8.68	0.15	1.490	
J175847.2–290711	104	113 18155 159	18.20	16.02			7.83	7.35	0.1	1.834	
J175847.5–290157	108	113 18156 54	16.47	14.66			8.54	8.37	0.15	1.768	
J175847.8–290943	111	113 18154 23	15.78	14.24			9.29	8.79	0.1	1.980	
J175848.0–291003	112	113 18154 20	16.17	14.06			7.33	7.26	0.3	2.342:	
J175848.2–290127	113	113 18156 279	18.74	16.39			7.72	6.52	0.3	2.145	
J175848.7–290743	117	113 18154 80	17.98	15.60			7.48	6.58	0.3	1.993	
J175849.2–291120	121	113 18154 26	16.53	14.64			8.02	6.74	0.5	2.581:	dp(0.15,1.756)
J175849.3–290528	124	113 18285 146	16.97	15.14			8.68	8.85	0.1	1.298	
J175849.5–291012	126	113 18284 606	18.98	16.65			8.41	7.47	1.0	2.344:	

Table 1—Continued

ISOGALP <sup>A</sup>	BW <sup>B</sup>	MACHO <sup>C</sup>	$V^D$	$R^D$	$J_0$	$K_0$	[7]	[15]	Amp.	$\log P^E$	notes <sup>F</sup>
J175850.2–290633	128	113 18285 55	14.93	13.61			8.52	8.40	0.1	2.145	
J175850.3–290455	129	113 18285 115	17.45	15.15			7.47	6.57	0.5	2.063	
J175850.6–291015	134	113 18284 413	18.14	16.01			7.64	6.53	0.5	2.094	
J175850.7–290314	135	113 18286 81	16.66	14.73			8.14	7.94	0.15	1.478	
J175850.9–290106	136	113 18286 615	18.61	16.70			7.54	5.51	0.35	2.158:	
J175851.2–290721	139	113 18285 35	15.02	13.40			7.60	6.99	0.4	1.852	
J175851.2–290206	140	113 18286 592	17.25	16.24			8.64	8.50	0.1	1.523	
J175851.6–290315	141	113 18286 54	15.69	14.15			8.15	8.20	0.08	1.185	
J175852.0–290524	143	113 18285 523	17.15	16.14			8.17	7.16	0.1	1.980	
J175853.3–290422	154	113 18285 314	17.69	15.74			8.57	8.35	0.3	1.523	
J175853.3–290831	155	113 18284 79	15.92	14.28			8.61	7.86	0.1	1.560	
J175853.6–285938	157	113 18287 1926	16.55	14.59			7.93	7.99	0.15	1.448	
J175854.2–290351	162	113 18285 61	15.70	14.13			8.74	8.50	0.1	1.390	
J175854.2–290523	163	113 18285 390	18.00	15.90			8.55	7.90	0.6	2.048	
J175854.5–291031	164	113 18284 188	17.89	15.62			7.51	6.63	0.4	1.922	
J175854.5–290323	165	113 18286 189	17.51	15.49			8.85	8.67	0.2	1.409	
J175854.8–285831	167	113 18287 1897	14.43	12.74			6.84	6.94	0.25	1.403	
J175854.9–290118	168	113 18286 24	9.71:	9.40:			7.46	7.76			
J175855.1–290037	169	113 18286 42	15.16	13.59			8.21	8.57	0.2	1.718	
J175855.1–290627	170	113 18285 564	17.79	16.21			6.99	5.53	0.15	2.127	
J175855.4–285808	172	113 18287 1899	14.33	13.13			8.94	8.61	0.1	1.240	
J175855.7–291208	174	113 18283 170	17.40	15.37			7.86	7.67	0.25	1.615	
J175855.7–290707	176	113 18285 138	17.08	15.11			8.00	7.73	0.2	1.672	
J175856.1–285943	183	113 18286 33	13.51:	12.24:			8.80	8.37			
J175856.4–290050	187	113 18286 454	19.08	16.46			6.73	5.37	0.3	2.299:	
J175856.7–290559	190	113 18285 133	16.93	15.07			8.68	8.37	0.15	1.448	
J175856.9–290339	194	113 18286 166	17.34	15.40			8.32	8.20	0.2	1.746	
J175857.0–290445	197	113 18285 148	17.39	15.17			7.62	7.14	0.3	1.649	
J175857.1–290804	198	113 18284 189	16.93	15.23			8.91	8.80	0.1	1.324	

Table 1—Continued

ISOGALP <sup>A</sup>	BW <sup>B</sup>	MACHO <sup>C</sup>	$V^D$	$R^D$	$J_0$	$K_0$	[7]	[15]	Amp.	$\log P^E$	notes <sup>F</sup>
J175857.4–291215	200	113 18283 439	16.97	15.88			7.20	6.11	0.12	2.006	
J175857.5–290537	202	113 18285 41	14.81	13.43			8.57	8.73	0.1	1.993	
J175857.6–290632	204	113 18285 39	14.78	13.41			8.65	8.60	0.5	1.776	
J175857.8–290114	206	113 18286 193	17.73	15.75			6.65	5.34	0.4	2.512:	
J175858.0–290349	208	113 18285 420	18.28	16.17			8.46	7.84	0.6	2.365:	
J175858.4–285636	214	113 18287 41	15.38:	13.89:			8.40	7.35			
J175858.5–291135	218	113 18284 54	14.91	13.61			9.01	8.81	0.1	1.303	
J175858.5–290845	219	113 18284 274	17.66	15.71			8.47	8.25	0.25	1.560	
J175858.6–290722	220	113 18285 65	15.96	14.23			8.59	8.47	0.2	1.691	
J175900.0–285813	234	113 18287 1906	15.10	13.74			8.43	7.69	0.1	1.229	
J175900.2–290556	235	113 18285 156	16.68	15.12			9.27	8.97	0.1	1.214	
J175900.2–291111	236	113 18284 59	16.23	14.50			7.85	7.44	01.0	2.164	
J175900.7–290305	242	113 18286 103	16.90	14.95			8.58	8.47	0.15	1.426	
J175900.9–290952	244	113 18284 834	18.74	16.67			8.28	7.13	0.4	1.912	
J175900.9–291238	245	113 18283 201	17.26	15.40			8.35	8.19	0.2	1.560	
J175901.1–285821	247	113 18287 2391	17.48	16.56			5.96	4.46			Mira/nil; sat
J175901.2–290910	249	113 18284 285	17.59	15.61			8.94	8.87	0.2	1.396	
J175901.2–290518	250	113 18285 296	17.89	15.83			8.07	7.29	0.15	1.800	
J175901.4–290802	252	113 18284 491	18.34	16.21			7.98	7.03	0.3	1.922	
J175902.0–290531	258	113 18285 157	17.17	15.22			8.23	8.50	0.2	1.555	
J175902.2–290625	261	113 18285 134	17.36	15.36			7.55	6.60	0.3	1.922	
J175903.0–290137	266	113 18286 150	16.48	15.07			9.86	8.09	0.25	1.523	
J175903.0–290842	267	113 18284 474	17.17	16.15			8.39	8.32	0.2	1.183	
J175903.2–291205	270	113 18283 48	15.45	13.94			8.51	8.51	0.15	1.637	
J175903.5–290603	273	113 18285 150	17.19	15.30			7.96	7.55	0.08	1.792	
J175903.5–290830	274	113 18284 39	13.51:	12.49:			8.63	8.66			
J175903.7–285919	277	113 18287 1968	16.56	15.07			8.77	8.79	0.15	1.444	
J175903.8–291126	278	113 18284 36	13.38:	12.00:			8.27	8.41			
J175904.0–290922	282	113 18284 37	13.57:	12.45:			8.38	8.43			



Table 1—Continued

ISOGALP <sup>A</sup>	BW <sup>B</sup>	MACHO <sup>C</sup>	$V^D$	$R^D$	$J_0$	$K_0$	[7]	[15]	Amp.	$\log P^E$	notes <sup>F</sup>
J175904.2–291103	288	113 18284 192	17.59	15.39			8.32	8.05	0.5	2.063	
J175904.7–290745	291	113 18284 284	16.92	15.43			7.02	5.65	0.3	2.103	
J175905.2–290708	294	113 18285 47	14.95	13.53			8.64	8.81	0.1	1.339	
J175905.6–285833	299	113 18287 2109	18.47	16.36			7.95	6.86	0.3	1.901	
J175905.6–290545	302	113 18285 44	14.65	13.37			8.88	8.72	0.1	1.273	
J175905.6–290235	303	113 18286 399	18.48	16.15			7.08	6.01	0.3	1.980	
J175905.7–291128	304	113 18284 389	18.34	16.38			8.84	8.74	0.5	1.303	
J175905.8–291105	308	113 18284 66	15.45	14.03			8.13	8.09	0.1	1.704	
J175906.0–290620	311	113 18285 45	15.21	13.71			8.46	8.55	0.3	1.776	
J175906.0–290732	312	113 18285 60	14.32	13.70			8.73	8.63	0.06	1.409	
J175906.5–290527	317	113 18285 107	16.59	14.87			8.04	8.04	0.15	1.459	
J175907.2–291259	326	113 18283 37	14.66	13.28			8.25	7.93	0.4	1.980	
J175907.3–291241	327	113 18283 141	16.97	15.12			8.63	8.58	0.15	1.470	
J175907.3–291024	328	113 18284 57	16.01	14.02			7.24	6.68	0.6	2.145	
J175908.1–285827	336	113 18417 2005	16.99	15.07			8.43	8.22	0.25	1.486	
J175908.3–290856	338	113 18414 98	17.19	15.01			7.46	6.40	0.6	2.084	
J175908.3–290729	339	113 18415 36	14.89	13.42			8.43	8.33	0.2	1.555	
J175908.6–291250	343	113 18413 45	15.73	14.08			8.25	8.11	0.1	1.216	
J175908.7–291345	345	113 18413 2532	19.05	18.12			7.86	7.73	0.35	1.968	
J175909.3–290423	350	113 18415 116	16.72	15.05			8.93	8.85	0.15	1.365	
J175909.5–290825	352	113 18414 49	16.09	14.23			7.48	7.31	0.2	1.615	
J175909.6–285800	353	113 18417 1984	15.90	14.36			8.98	8.83	0.1	1.383	
J175910.1–290936	357	113 18414 26	11.85:	11.00:			8.72	8.77			
J175910.1–291358	358	113 18413 59	16.34	14.49			8.32	7.72	0.35	1.746	
J175910.5–290129	363	113 18416 198	19.83	16.44			4.87	3.37		2.672:	Mira; few
J175910.6–290457	365	113 18415 117	17.54	15.25			7.24	6.45	0.4	2.145	
J175910.7–290035	370	113 18416 80	15.99	14.24			7.99	7.81	0.2	1.724	
J175910.9–290708	372	113 18415 43	15.37	13.87			8.15	8.07	0.25	1.637	
J175910.9–285747	373	113 18417 1968	15.66	14.00			8.45	8.47	0.2		also long per

Table 1—Continued

ISOGALP <sup>A</sup>	BW <sup>B</sup>	MACHO <sup>C</sup>	$V^D$	$R^D$	$J_0$	$K_0$	[7]	[15]	Amp.	$\log P^E$	notes <sup>F</sup>
J175911.1–290315	375	113 18416 597	18.27	16.50			6.71	5.34	0.5	2.201:	
J175911.1–291401	376	113 18413 410	18.35	16.25			7.87	6.95	0.35	2.110	
J175911.3–290114	380	113 18416 29	10.04:	9.64:			7.51	7.19			
J175912.4–291357	388	113 18413 60	15.98	14.27			8.21	8.37	0.1	1.448	
J175912.7–290608	392	113 18415 112	16.94	15.02			8.48	8.50	0.25	1.490	
J175913.2–290901	395	113 18414 198	17.78	15.62			7.81	7.15	0.25	1.852	
J175913.5–291409	399	113 18413 125	16.92	15.00			8.45	8.35	0.15	1.416	
J175913.6–285812	400	113 18417 1956	14.18	12.62			7.36	7.10	0.4	1.980	
J175913.7–285852	402	113 18417 1965	19.49	16.44			6.96	5.75	4.0	2.487:	Mira
J175913.8–290703	403	113 18415 100	16.78	14.98			8.78	8.32	0.15	1.514	
J175914.0–290950	405	113 18414 551	18.27	16.28			7.14	5.58	0.3	2.063	
J175914.0–290815	406	113 18414 137	17.03	15.12			8.75	8.95	0.15	1.356	
J175914.1–290241	407	113 18416 337	18.02	15.98			8.00	7.16	0.35	1.852	
J175914.4–291335	410	113 18413 19	13.03:	11.80:			7.21	6.80			
J175914.6–290853	412	113 18414 39	14.12	13.54			8.80	8.62	0.1	1.433	
J175914.8–291129	416	113 18414 338	18.13	15.86			7.40	6.41	0.4	1.970	
J175915.5–290134	421	113 18416 1364	18.05	17.60			6.80	6.07	0.4	1.159	few
J175915.5–290533	422	113 18415 74	17.16	14.86			7.60	6.80	0.5	1.901	
J175915.9–290824	425	113 18414 177	17.42	15.33			7.87	7.78	0.2	1.816	
J175915.9–290839	426	113 18414 61	16.16	14.25			7.64	7.59	0.25	1.724	
J175916.0–290408	427	113 18415 71	16.36	14.56			8.66	8.53	0.15	1.738	
J175916.4–290805	431	113 18414 211	17.35	15.31			7.57	6.75	0.25	1.808	
J175916.8–290011	434	113 18416 28	9.75:	9.42:			7.24	7.38			
J175916.9–290225	435	113 18416 138	16.08	14.83			9.16	8.73	0.05	1.163	
J175917.0–290502	439	113 18415 39	14.43	13.27			9.04	8.85	0.2	1.753	
J175917.4–290643	442	113 18415 24	13.36:	12.04:			7.76	7.76			
J175917.4–291048	444	113 18414 56	16.55	14.43			7.58	6.93	0.7	2.185:	
J175917.9–290806	447	113 18414 290	18.22	15.92			7.53	6.48	0.3	1.945	
J175918.2–291434	452	113 18413 20	13.42:	11.98:			6.66	6.50			

Table 1—Continued

ISOGALP <sup>A</sup>	BW <sup>B</sup>	MACHO <sup>C</sup>	$V^D$	$R^D$	$J_0$	$K_0$	[7]	[15]	Amp.	$\log P^E$	notes <sup>F</sup>
J175918.2–290123	453	113 18416 40	14.36	12.64			6.07	5.83	0.45	1.579	
J175918.5–291302	454	113 18413 33	14.96	13.70			8.65	8.81	0.1	2.145	
J175918.5–290505	455	113 18415 73	16.73	14.58			7.29	6.58	0.8	2.124:	
J175918.5–290608	457	113 18415 415	18.73	16.34			7.32	5.77	0.4	2.097:	
J175918.6–290046	458	113 18416 49	14.75	13.44			8.75	8.74	0.15	1.399	
J175918.9–290548	463	113 18415 62	15.76	14.30			8.94	8.64	0.08	1.209	
J175919.6–290452	467	113 18415 26	14.17	12.95			8.50	8.42	0.15	1.776	
J175919.8–291247	469	113 18413 56	15.65	14.15			8.77	8.80	0.15	1.448	
J175920.1–291416	471	113 18413 670	17.93	17.37			8.48	8.42	1.0	1.834	
J175920.6–290953	477	113 18414 1489	19.00	17.78			9.06	8.10	0.9	2.078	
J175920.7–291506	478	113 18413 167	17.45	15.34			7.37	7.07	0.25	1.834	
J175921.8–290841	486	113 18414 97	16.75	14.84			8.35	8.39	0.35	1.717	
J175921.9–291058	487	113 18414 96	16.78	14.86			7.88	7.79	0.25	1.654	
J175922.0–291229	488	113 18413 21	14.65	12.84			6.46	6.03	0.35	1.816	
J175922.0–290547	490	113 18415 83	16.56	14.69			8.32	8.15	0.35	1.724	
J175922.1–291157	492	113 18413 1433	18.66	17.49			8.82	8.11	0.4	1.944	
J175922.5–291133	500	113 18414 95	16.57	14.76			8.80	8.68	0.25	1.792	
J175923.2–290820	506	113 18414 34	14.71	13.34			8.54	8.31	0.3	1.871	
J175923.3–290902	510	113 18414 27	12.33:	10.78:			8.22	8.19			
J175923.4–290216	511	113 18416 290	16.67	15.56			6.37	5.39			Mira; sat
J175923.5–291451	512	113 18413 317	18.33	16.08			8.00	7.44	1.0	2.117:	
J175923.7–291236	514	113 18413 1776	18.94	17.04			6.83	5.64	4	2.405:	Mira
J175923.8–290952	516	113 18414 93	16.70	14.94			8.85	8.84	0.2	1.490	
J175924.4–291358	522	113 18413 31	15.54	13.60			7.24	6.21	0.4	1.896	
J175924.6–291237	524	113 18413 206	18.40	15.88			7.47	6.15	0.5	2.020	
J175925.3–290336	529	113 18416 521	18.40	16.43			7.13	5.70	0.25	2.110	
J175925.7–290036	533	113 18416 58	15.20	13.78			8.96	8.77	0.15	1.594	
J175926.1–290612	536	113 18545 1157	18.47	17.06			8.20	7.90	0.25	1.791	
J175926.4–290707	540	113 18545 19	15.14	13.34			7.03	5.84	0.35	1.718	

Table 1—Continued

ISOGALP <sup>A</sup>	BW <sup>B</sup>	MACHO <sup>C</sup>	$V^D$	$R^D$	$J_0$	$K_0$	[7]	[15]	Amp.	$\log P^E$	notes <sup>F</sup>
J175926.5–290218	541	113 18546 277	17.34	15.46			7.34	5.60	0.2	1.891	
J175926.9–290345	545	113 18545 273	16.87	15.63			9.18	8.62	0.06	1.205	
J175927.4–290310	550	113 18546 982	19.17	17.80			7.46	5.91			eclip bin
J175927.7–291332	553	113 18543 48	16.14	14.41			8.39	8.23	0.1	1.191	
J175927.9–290530	556	113 18545 233	17.92	15.71			7.46	6.61	0.3	1.861	
J175927.9–291038	559	113 18544 65	16.85	14.85			7.76	7.62	0.3	1.615	
J175928.0–290118	561	113 18546 36	14.49	13.18			8.38	8.19	0.1	1.760	
J175929.7–290926	575	113 18544 13	13.76	12.64			8.46	8.37	0.2	2.164	sat?
J175930.7–290950	581	113 18544 12	11.80:	11.60:			6.88	6.83	0.3		
J175931.1–290858	585	113 18544 399	18.04	16.13			7.05	5.67	0.3	2.083:	
J175932.1–290857	595	113 18544 26	15.51	13.90			8.32	7.67	0.3	2.020	
J175932.4–290802	598	113 18544 474	16.90	16.07			7.99	7.91	0.1	1.311	
J175934.0–290727	611	113 18545 927	17.38	16.53			8.64	8.57	0.06	1.110	
J175935.0–291110	619	113 18544 255	16.54	15.64			8.26	7.64	0.08	1.154	
J175935.2–290506	623	113 18545 81	14.79	14.34			8.56	8.74	0.05	1.980	
J175936.1–290916	626	113 18544 21	15.60	13.61			6.96	6.75	0.4	2.145	
J175936.3–290516	628	113 18545 740	17.36	16.38			8.30	7.64	0.1	1.079	
J175937.0–290835	633	113 18544 131	17.46	15.48			7.44	6.56	0.6	2.110	
J175937.1–290253	634	113 18546 458	16.78	16.04			8.34	8.32	0.05	1.753	
J175937.8–290925	639	113 18544 36	15.60	14.18			8.81	8.74	0.25	1.283	
J175938.3–290129	644	113 18546 279	16.68	15.66			7.92	7.34	0.06	2.020	
J175939.3–290915	655	113 18544 61	16.72	14.69			8.58	8.39	0.2	1.649	
J175940.9–290737	661	113 18545 532	17.03	16.10			8.41	8.36	0.06	1.968	
J175941.9–290458	667	113 18545 33	13.95	13.49			8.25	8.28	0.03	1.039	
J175943.4–290735	672	113 18545 228	16.25	15.34			7.88	7.03	0.05	1.451	
J175947.0–290357	687	113 18675 756	17.17	16.31			7.65	7.02	0.25	1.079	
J175948.2–290350	689	113 18675 1135	17.62	16.70			7.05	6.37	0.15	2.033	definite mis-id
J180232.1–300201	6	119 19831 41	14.85	13.71			8.63	8.56	0.06	1.213	
J180233.9–300232	8	119 19831 110	16.14	14.99			9.94	8.89	0.05	1.386	

Table 1—Continued

ISOGALP <sup>A</sup>	BW <sup>B</sup>	MACHO <sup>C</sup>	$V^D$	$R^D$	$J_0$	$K_0$	[7]	[15]	Amp.	$\log P^E$	notes <sup>F</sup>
J180235.2–295855	14	119 19832 2797	14.75	12.73			6.50	5.78	0.1	1.951	
J180236.1–300216	17	119 19831 173	17.54	15.62			8.99	8.50	0.2	1.422	
J180236.6–295752	19	119 19832 2843	16.95	15.03			7.81	7.54	0.2	1.455	few
J180238.0–295933	22	119 19832 2832	16.54	14.78			8.80	8.76	0.15	1.625	
J180238.7–295954	24	119 19831 471	18.18	16.59			7.75	6.25	0.35	2.075	
J180239.4–295918	25	119 19832 2808	15.22	13.80			8.93	8.78	0.1	1.361	
J180239.4–295636	26	119 19832 18	11.96:	10.35:			7.46	7.16			
J180240.2–295821	27	119 19832 2805	15.40	13.87			7.96	7.78	0.15	1.625	
J180240.6–300053	28	119 19831 75	16.51	14.67			8.16	8.02	0.15	1.433	
J180241.0–295902	31	119 19832 2872	17.83	15.80			8.80	8.43	0.2	2.060	
J180241.7–295753	35	119 19832 2804	15.38	13.83			8.54	8.27	0.2	1.716	few
J180241.8–295957	36	119 19831 139	17.40	15.52			8.25	7.91	0.3	1.990	
J180242.1–295937	38	119 19832 2794	12.25:	11.25:			8.28	8.19			
J180242.9–300335	41	119 19831 494	19.06	16.88			7.48	5.86	0.5	2.106	
J180243.5–295615	45	119 19832 45	16.88	15.02			8.36	8.25	0.25	1.625	
J180245.1–295813	53	119 19832 2824	16.01	14.52			9.28	8.99	0.1	1.256	
J180245.4–295536	57	119 19833 45	14.57	13.51			8.40	8.25	0.5	1.249	
J180245.6–300328	60	119 19831 49	15.62	14.14			8.99	8.86	0.06	1.703	
J180245.8–300111	61	119 19831 299	18.22	16.22			7.58	6.00	0.35	2.060	BMB3 7
J180248.4–300309	70	119 19961 106	17.46	15.40			8.12	7.69	0.3	1.759	
J180249.0–295430	76	119 19963 151	17.75	15.65			8.00	7.02	0.4	1.899	
J180249.5–295852	79	119 19962 2779	16.22	14.63			8.53	8.06	0.3	1.798	BMB6 6
J180251.1–300326	83	119 19961 18	12.74:	12.47:			8.31	8.25			
J180251.2–300013	85	119 19961 64	17.30	15.14			7.49	6.61	0.7	1.943	BMB7 7
J180251.8–300246	88	119 19961 132	17.41	15.32			8.11	7.65	0.25	1.767	
J180252.4–300023	90	119 19961 163	17.80	15.70			8.57	7.87	0.3	2.060	BMB12 6
J180252.7–295459	92	119 19963 178	17.78	15.76	9.64	8.47	8.72	8.65	0.2	1.555	BMB11 7; few
J180252.9–300106	94	119 19961 146	18.05	15.92			8.36	7.63	0.4	2.004	BMB10 6.5
J180253.0–300249	96	119 19961 162	17.60	15.53			7.51	6.66	0.3	1.920	

Table 1—Continued

ISOGALP <sup>A</sup>	BW <sup>B</sup>	MACHO <sup>C</sup>	$V^D$	$R^D$	$J_0$	$K_0$	[7]	[15]	Amp.	$\log P^E$	notes <sup>F</sup>
J180253.8–295425	102	119 19963 60	16.10	14.48			8.25	8.16	0.15	1.554	BMB15 6
J180254.1–300048	103	119 19961 84	17.03	14.89			7.65	6.65	0.5	1.899	BMB12 6
J180256.1–295534	110	119 19963 138	18.08	15.73			6.71	5.77	0.5	2.447:	
J180256.7–295705	114	119 19962 23	15.11	13.63			8.47	8.14	0.5	1.869	
J180256.9–295548	118	119 19962 99	16.79	15.71			7.63	7.32	0.15	1.444	BMB20/21 6/6.5
J180257.2–295201	121	119 19963 67	16.07	14.54			9.24	8.75	0.1	1.631	
J180257.4–300351	126	119 19960 22	13.97	12.77			8.27	7.69	0.1	1.625	
J180257.6–295124	128	119 19964 19	13.07:	12.25:			6.80	6.32			
J180258.1–295049	131	119 19964 25	14.47	13.17			8.36	8.14	0.15	1.365	
J180258.4–300311	135	119 19961 108	17.20	15.26			8.38	8.49	0.2	1.767	
J180258.8–295426	136	119 19963 30	15.29	13.77			8.23	6.95	0.5	2.581:	dp(0.2,1.869)
J180258.9–295221	138	119 19963 32	14.86	13.57			8.88	8.77	0.08	1.554	
J180258.9–300108	139	119 19961 71	16.64	14.87			8.70	8.56	0.25	1.554	BMB27 6.5
J180259.0–295757	140	119 19962 2777	16.28	14.45			8.01	7.40	0.3	2.004	
J180259.6–300253	147	119 19961 176	17.71	15.64	8.47	7.23	7.03	5.28	0.4	2.371:	BMB28 7
J180300.2–295514	152	119 19963 15	12.27:	10.84:			7.81	7.55			
J180300.6–295018	156	119 19964 22	14.40	12.93			8.27	7.63	0.05	1.919	
J180301.1–300142	162	119 19961 20	15.33	13.07			6.36	5.51	0.1	2.004	
J180301.7–295959	166	119 19961 155	17.58	15.63			8.31	8.09	0.25	1.527	BMB35 6.5
J180301.7–295053	167	119 19964 38	14.62	13.59			9.02	8.60	0.1	1.103	
J180302.6–295645	172	119 19962 28	16.30	14.43			7.96	7.44	0.6	2.091	BMB37 6
J180303.2–295515	179	119 19963 20	14.24	12.83			8.48	8.60	0.06	1.823	
J180303.8–300242	183	119 19961 130	17.25	15.31			8.50	7.88	0.5	1.850	BMB36 6.5
J180304.0–295135	184	119 19964 79	16.35	14.71			9.03	8.55	0.1	2.090	BMB44 6.5
J180304.6–300405	187	119 19960 39	15.53	14.15			8.60	8.32	0.2	1.645	
J180304.9–295258	189	119 20093 2040	17.18	15.29			8.43	8.31	0.15	1.573	
J180305.3–295516	192	119 20093 2054	17.71	15.51	8.35	7.00	6.86	5.52	0.3	2.060	BMB46 7
J180305.4–295033	194	119 20094 1986	13.75	12.58			8.06	7.68	0.05	1.204	
J180305.9–295345	197	119 20093 2027	16.37	14.78			9.09	8.48	0.4	1.824	

Table 1—Continued

ISOGALP <sup>A</sup>	BW <sup>B</sup>	MACHO <sup>C</sup>	$V^D$	$R^D$	$J_0$	$K_0$	[7]	[15]	Amp.	$\log P^E$	notes <sup>F</sup>
J180305.9–300508	198	119 20090 51	16.70	14.91			8.87	8.83	0.2	1.370	
J180306.3–295204	205	119 20093 2179	18.38	16.42			7.40	5.75	0.2	2.142	
J180306.3–295141	206	119 20094 2053	17.29	15.29			7.82	6.75	0.4	1.910	BMB50 7
J180306.7–300136	207	119 20091 8	12.47:	11.02:			8.62	8.62			
J180307.0–300633	211	119 20090 106	18.04	16.00			7.93	7.09	0.2	1.888	BMB45 7
J180307.1–300519	213	119 20090 118	18.26	16.08			8.60	7.55	0.4	1.866	BMB49 6.5
J180307.4–300255	215	119 20091 11	14.60	13.29			8.45	8.31	0.25	1.609	
J180307.8–300452	217	119 20090 26	15.15	13.88			9.16	8.82	0.05	2.075	
J180308.2–300330	221	119 20091 95	17.23	15.64			8.22	7.71	0.2	1.966	BMB53 6.5
J180308.5–300525	224	119 20090 355	18.97	16.68	8.41	6.94	6.32	4.82	4.0	2.531:	Mira; BMB54 7
J180308.8–295220	226	119 20093 2095	18.17	16.02			7.83	6.43	0.3	1.991	BMB59 6.5
J180308.9–300551	227	119 20090 43	16.06	14.64			9.45	8.75	0.1	1.292	
J180309.3–295241	231	119 20093 1994	15.15	13.71			8.04	7.97	0.2	1.631	
J180309.4–300241	234	119 20091 13	14.55	13.45			8.86	8.83	0.1	1.292	
J180310.0–300138	236	119 20091 27	15.95	14.51			8.66	8.45	0.1	1.473	BMB58 6
J180310.6–295619	240	119 20092 756	15.85	14.66			9.30	8.49	0.15	1.079	
J180311.2–295312	242	119 20093 1991	14.41	13.01			8.09	7.79	0.6	1.850	
J180311.9–295900	248	119 20092 2338	13.89	12.74			9.09	8.73	0.05	1.598	
J180312.5–300429	254	119 20090 55	17.48	15.23			7.04	5.98	0.4	1.954	BMB54 7
J180313.4–300056	256	119 20091 153	19.23	16.41			7.38	6.35	0.7	2.346:	BMB67 8
J180313.9–295620	259	119 20092 748	15.93	14.16			8.02	7.36	0.4	1.876	
J180317.9–300230	292	119 20091 3890	17.02	15.29			8.86	8.58	0.3	2.060	BMB79 6.5
J180318.1–300309	294	119 20091 3853	16.03	14.51	10.10	9.09	9.30	8.85	0.1	1.943	BMB84 6
J180318.4–295346	299	119 20093 55	17.57	15.81	8.64	7.29	7.15	5.29	0.2	1.879	BMB86 9; long per?
J180320.1–295935	313	119 20092 4026	15.32	13.83			8.64	8.35	0.1	1.088	BMB89 5
J180320.3–295432	317	119 20093 31	16.36	14.79	9.41	8.37	8.62	8.57	0.1	1.389	BMB91 6.5
J180320.8–300451	319	119 20090 3751	17.29	15.42			9.12	8.66	0.15	1.396	
J180322.3–300255	333	119 20091 3839	14.88	13.22	8.23	7.18	7.43	7.08	0.25	1.710	BMB93 6
J180323.4–300838	339	119 20219 52	16.97	14.97			7.58	6.20	1.0	2.091	

Table 1—Continued

ISOGALP <sup>A</sup>	BW <sup>B</sup>	MACHO <sup>C</sup>	$V^D$	$R^D$	$J_0$	$K_0$	[7]	[15]	Amp.	$\log P^E$	notes <sup>F</sup>
J180323.9–295410	346	119 20223 112	17.18	15.15			8.08	6.92	0.35	1.943	BMB103 6.5
J180323.9–300004	347	119 20221 80	15.73	14.33	10.04	9.04	9.14	8.74	0.5	2.602:	B28 5; dp(0.1,1.7)
J180324.0–295925	350	119 20222 2570	17.59	15.57			8.16	7.97	0.3	1.790	BMB101 6.5
J180324.5–300414	354	119 20220 61	16.18	14.41	9.32	8.27	8.71	8.83	0.1	1.518	BMB99 6.5
J180325.1–300849	357	119 20219 54	15.13	14.14			9.22	8.56	0.03	1.370	
J180325.3–300645	360	119 20220 54	16.22	14.37			8.43	8.56	0.4	1.790	BMB102 6.5
J180325.3–295947	361	119 20221 104	16.79	14.70	9.36	8.29	8.51	8.46	0.15	1.573	BMB106 6
J180325.8–295847	365	119 20222 2546	16.83	14.84	8.54	7.51	7.54	6.89	0.7	2.060	BMB108 6
J180326.3–295653	368	119 20222 12	13.44:	12.52:			8.27	8.25			
J180326.4–300700	370	119 20220 395	16.98	16.02			8.91	8.38	0.15	1.455	
J180327.3–300102	375	119 20221 126	16.91	14.81	8.80	7.65	7.78	7.10	0.3	1.824	BMB114 6.5
J180327.5–300224	379	119 20221 55	15.23	13.65	9.09	8.09	8.29	8.71	0.1	1.220	B47 5
J180327.7–300655	381	119 20220 158	16.75	15.41			9.50	8.37	0.15	2.107	
J180328.4–295545	382	119 20222 81	18.30	16.02			7.25	5.54	0.1	2.030	BMB119 9
J180328.9–300334	386	119 20221 30	12.74:	11.28:			8.81	8.90			
J180329.3–300248	387	119 20221 45	14.16	12.97			8.61	8.72	0.35	1.767	B54 1 bl?
J180329.4–295939	389	119 20222 2540	16.38	15.11	8.58	7.31	7.38	5.99	0.1	2.075	BMB120 7
J180329.6–300108	394	119 20221 108	16.51	14.63			7.92	7.25	0.5	1.943	BMB121 6.5
J180330.0–295821	397	119 20222 2501	14.71	13.30			8.43	8.21	0.25	1.603	B61 5
J180331.0–295846	405	119 20222 2498	13.16:	12.08:			9.40	8.49			
J180331.1–295908	407	119 20222 2573	17.61	15.46	9.26	8.12	8.41	7.51	0.2	1.806	BMB127 7
J180331.2–295333	409	119 20223 158	17.29	15.35	8.77	7.56	7.75	7.64	0.2	1.910	BMB136 8
J180331.3–300101	410	119 20221 39	15.02	13.10			6.71	6.33	0.2	1.625	BMB129 6.5
J180331.6–300043	413	119 20221 44	14.20	13.03	9.58	8.74	8.98	8.77	0.06	1.568	B66 3
J180331.9–300608	414	119 20220 50	16.35	14.39	8.93	7.85	8.01	7.36	0.3	2.060	BMB128 7
J180331.9–300027	415	119 20221 56	15.35	13.65	8.81	7.79	8.17	8.13	0.25	1.638	BMB131 6
J180332.3–300147	418	119 20221 60	15.20	13.71			8.91	8.60	0.1	2.031	BMB133 6
J180332.3–300444	419	119 20220 81	16.34	14.61	9.77	8.71	8.82	8.73	0.3	1.416	BMB133 6
J180333.2–295910	425	119 20222 2518	17.19	15.12			8.37	7.56	1.0	2.316:	BMB140 6.5



Table 1—Continued

ISOGALP <sup>A</sup>	BW <sup>B</sup>	MACHO <sup>C</sup>	$V^D$	$R^D$	$J_0$	$K_0$	[7]	[15]	Amp.	$\log P^E$	notes <sup>F</sup>
J180333.4–300523	426	119 20220 89	15.98	14.73	9.23	8.06	8.86	7.39	0.2	1.869	BMB134 7
J180334.1–295957	432	119 20221 178	17.52	15.30	8.17	6.90	6.97	5.56	0.35	2.075	BMB142 8
J180334.2–300104	433	119 20221 88	16.34	14.39			7.71	7.15	0.2	2.004	BMB143 6.5
J180334.6–300137	437	119 20221 100	16.48	14.57			8.36	8.35	0.2	1.760	BMB146 6; few
J180336.9–300148	445	119 20221 290	16.23	15.42	8.51	7.21	7.07	6.03	0.2	1.043	BMB152 9
J180339.1–295826	456	119 20222 2502	14.77	13.55			9.23	8.99	0.1	1.737	B101 4
J180340.2–295531	459	119 20223 43	14.75	13.35			8.04	8.24	0.2	1.473	
J180340.4–295612	460	119 20222 19	15.80	14.40			9.26	8.91	0.15	1.258	
J180342.9–295606	467	119 20352 15	10.41:	9.94:			8.62	8.62			BMB156 6
J180345.1–295516	473	119 20353 289	16.73	15.77			0.44	8.91	0.05	1.412	
J180346.2–295912	476	119 20352 2239	17.60	15.41	8.20	6.87	7.00	5.21	0.3	2.075	BMB179 7
J180348.5–295946	483	119 20351 63	16.77	14.60			7.79	7.09	0.25	1.850	BMB186 6.5
J180350.9–295618	491	119 20352 38	18.76	16.79	7.61	6.44	6.31	5.26	4.0	2.498:	BMB194 6.5; Mira

<sup>A</sup> The full ISOGAL designation is of the form: ISOGALP Jhhmmss.s-ddmmss (2000). P signifies ‘provisional’.

<sup>B</sup> BW denotes the running number during the analyses of the Sgr I and NGC6522 fields.

<sup>C</sup> The MACHO 3-digit identifier refers to the field, tile, and the sequence number (see Alcock et al. 1999).

<sup>D</sup> $V$  and  $R$  mags are flux-weighted time-averages. Those marked with “:” are by-eye estimates; these MACHO lightcurves show saturation effects. In these cases, no estimates for Amp. and  $\log P$  are given.

<sup>E</sup>Periods are in days. Those marked with “:” are by-eye estimates for some long-period variables as described in the text.

<sup>F</sup>BMB denotes Blanco McCarthy Blanco (1984), B denotes Blanco (1986), and the following number is the M giant spectral sub-type. Those marked with “Mira” are also listed in Table 1. In some cases we note a second or “double” period using the notation: dp(Amp. , $\log P$ ).

Table 2. Mira variables in the survey area

Name	MACHO	[7] <sub>avg</sub>	[15]	$K_{avg}$	Period <sup>1</sup>
NGC 6522					
TLE D9	missing <sup>2</sup>	4.96	3.64	5.78	
TLE228	missing <sup>2</sup>	6.03	5.11	6.60	
TLE403	119 20090 355	6.32	4.82	7.00	340/335
TLE238	missing <sup>2</sup>	6.84	5.80	7.44	
TLE136	119 20352 38	6.31	5.26	6.44	315/270
SGR I					
TLE65	113 18155 43	6.33	5.28	6.98	296/265
TLE79	113 18287 2391	5.96	4.46	6.66	mis-id <sup>4</sup>
TLE53	113 18416 198	4.87	3.37	6.43	470/500:: <sup>3</sup>
TLE87	113 18417 1965	6.96	5.75	7.29	307/315
TLE54	113 18416 290	6.37	5.39	7.04	mis-id <sup>4</sup>
TLE39	113 18413 1776	6.83	5.64	7.80	254/235
TLE55	missing <sup>2</sup>	6.51	5.47	6.81	-
TLE57	missing <sup>2</sup>	7.24	6.97	8.18	-
TLE56	113 18675 1135	7.05	6.37	7.43	mis-id <sup>4</sup>

Notes:

<sup>1</sup>The left period was derived from MACHO data and the right by Lloyd Evans (1976).

<sup>2</sup>“missing” stars probably appeared constant or non-stellar in the MACHO data due to saturation, and were rejected before the matching stage.

<sup>3</sup> fragmentary MACHO light curve.

<sup>4</sup> An apparent MACHO counterpart was mistakenly found during the cross-identification process; the image of the correct star was probably saturated.

Table 3. Spectral Energy Distribution Modeling Results

BW	MACHO	FW87	$M_{\text{bol}}$	$T_{(V-K)}$	$T_{\text{mod}}$	$\dot{M}_{\text{L4}}$	$\dot{M}$	x[15]	$V_{\text{exp}}$
92	119 19963 178	11	-3.12	3077	2500	1.0e-7	2.3e-8	0.79	13.6
147	119 19961 176	28	-4.35	2912	3000	8.2e-7	4.4e-7	129.65	16.2
192	119 20093 2054	46	-4.47	2882	3000	8.2e-7	4.8e-7	92.79	16.6
294	119 20091 3853	84	-2.69	3442	3500	6.8e-8	1.2e-8	2.23	14.4
299	119 20093 55	86	-4.18	2939	3000	8.2e-7	3.9e-7	131.36	15.6
317	119 20093 31	91	-3.37	3273	3200	5.4e-8	1.5e-8	0.72	15.1
333	119 20091 3839	93	-4.53	3318	3350	6.3e-8	3.8e-8	9.51	21.3
347	119 20221 80	B28	-2.84	3489	3500	1.4e-7	2.6e-8	2.27	14.8
354	119 20220 61	94	-3.39	3286	3350	6.3e-8	1.7e-8	-0.37	16.4
361	119 20221 104	106	-3.38	3197	3200	1.1e-7	3.0e-8	0.80	15.1
365	119 20222 2546	108	-4.19	3076	2500	1.9e-7	9.1e-8	17.36	16.3
375	119 20221 126	114	-3.98	3085	2500	1.9e-7	7.9e-8	14.74	15.5
379	119 20221 55	B47	-3.69	3408	3350	3.1e-8	1.1e-8	-2.70	17.6
389	119 20222 2540	120	-4.20	3113	3000	4.0e-7	1.9e-7	61.22	16.1
407	119 20222 2573	127	-3.43	3051	2500	1.9e-7	5.4e-8	12.01	13.7
409	119 20223 158	136	-3.98	3016	2500	1.9e-7	7.9e-8	2.58	15.5
413	119 20221 44	B66	-3.38	3805	3750	4.2e-8	1.2e-8	1.40	18.7
415	119 20221 56	131	-3.95	3339	3350	6.3e-8	2.6e-8	0.98	18.6
414	119 20220 50	128	-3.82	3197	3200	2.1e-7	7.8e-8	11.26	15.6
419	119 20220 81	133	-2.95	3329	3350	1.3e-8	2.7e-8	0.84	14.7
426	119 20220 89	134	-3.58	3284	3350	2.5e-7	7.9e-8	17.29	15.9
432	119 20221 178	142	-4.58	2894	3000	8.2e-7	5.2e-7	91.57	17.1
445	119 20221 290	152	-4.27	3120	3000	4.0e-7	2.0e-7	50.96	16.4
476	119 20352 2239	179	-4.59	2880	3000	8.2e-7	5.2e-7	139.46	17.1
491	119 20352 38	194	-5.06	2718	3000	3.3e-6	2.9e-6	104.12	16.3
224	119 20090 355	TLE403	-4.51	2741	3000	3.3e-6	2.0e-6	186.07	14.3